

Clinopyroxene/melt trace-element-partitioning in sodic alkaline magmas

Charles Beard^{a,*}, Vincent van Hinsberg^a, John Stix^a, Max Wilke^{b,c}

^a*Earth and Planetary Sciences, McGill University, 3450 University Street, Montreal, Québec, H3A 0E8, Canada*

^b*Institut für Erd- und Umweltwissenschaften, Universität Potsdam, Golm, Germany*

^c*Chemie und Physik der Geomaterialien, Deutsches GeoForschungsZentrum GFZ, Potsdam, Germany*

Abstract

Clinopyroxene is a key fractionating phase in alkaline magmatic systems, but its impact on metal-enrichment processes, and the formation of REE + HFSE mineralisation in particular, are not well understood. To constrain the control of clinopyroxene on REE + HFSE behaviour in sodic (per)alkaline magmas, a series of internally heated pressure vessel experiments was performed to determine clinopyroxene-melt element-partitioning systematics. Synthetic tephriphonolite to phonolite compositions were run H_2O -saturated at 650–825°C with oxygen fugacity buffered to $\log f\text{O}_2 \approx \Delta\text{QFM} + 1$ or $\log f\text{O}_2 \approx \Delta\text{QFM} + 5$. Clinopyroxene-glass pairs from basanitic to phonolitic fall deposits from Tenerife, Canary Islands, were also measured to complement our experimentally derived data set.

The REE partition coefficients are 0.3–53, typically 2–6, with minima for high-aegirine clinopyroxene. Diopside-rich clinopyroxene (Ae_{5--25}) prefer the

*corresponding author

Email address: charles.beard@mail.mcgill.ca (Charles Beard)

MREE and have high REE partition coefficients (D_{Eu} up to 53, D_{Sm} up to 47). As clinopyroxene become more Na- and less Ca-rich (Ae₂₅₋₋₅₀), REE incorporation becomes less favourable, and both the M1 and M2 sites expand (to 0.79 Å and 1.12 Å), increasing D_{LREE}/D_{MREE} . Above Ae₅₀, both M sites shrink slightly and HREE ($V^I r_i \leq 0.9 \text{ \AA} \approx \text{Y}$) partition strongly onto the M1 site, consistent with a reduced charge penalty for REE \leftrightarrow Fe³⁺ substitution.

Our data, complemented with an extensive literature database, constrain a model that predicts trace-element-partition coefficients between clinopyroxene and silicate melt using only mineral major-element compositions, temperature and pressure as input. The model is calibrated for use over a wide compositional range and can be used to interrogate clinopyroxene from a variety of natural systems to determine the trace-element concentrations in their source melts, or to forward model the trace-element evolution of tholeiitic mafic to evolved peralkaline magmatic systems.

Keywords: rare earth elements, aegirine, experimental petrology, Canary Islands, phonolite, peralkaline

1. Introduction

Sodic clinopyroxene appear to more readily incorporate REE than their calcic equivalents (Marks et al., 2004), but despite fractionation of these minerals, melts in evolved alkaline systems can attain high REE contents, even up to economic levels (Kogarko, 1990; Downes et al., 2005; Marks et al., 2011; Sjöqvist et al., 2013; Goodenough et al., 2016; Möller and Williams-Jones, 2016). Trace-element data may be used to model magmatic processes (Spera and Bohrson, 2001; Troll and Schmincke, 2002; Boudreau, 2004; Xu et al., 2010; Girnis et al., 2013; Mungall and Brenan, 2014), but their interpretation requires precise knowledge of mineral/liquid element-partition coefficients. The approach has been applied to studies of mafic systems and mantle melting processes (Niu, 2004; Workman and Hart, 2005; Foley et al., 2013; Coumans et al., 2016; Peters et al., 2017). However, poor constraints on element-partitioning behaviour in alkaline and peralkaline rocks thus far preclude widespread application in these systems.

Experimental investigations of element-partitioning behaviour in alkali-enriched systems are limited in terms of composition (Wood and Trigila, 2001; Huang et al., 2006), and none yet have explored peralkaline conditions where molar $(\text{Na}+\text{K})/\text{Al}$ exceeds 1. Additional information has been obtained from natural samples by measuring the concentration ratios of phenocryst–glass pairs from volcanic and intrusive rocks (Larsen, 1979; Wörner et al., 1983; Shearer and Larsen, 1994; Severs et al., 2009; Fedele et al., 2009; Mollo et al., 2016). However, these results may be biased by the presence of melt inclusions, mineral inclusions and mineral zoning, and their interpretation is commonly complicated by unknown or poorly constrained P-T-H₂O-*f*O₂ con-

²⁶ ditions of equilibration and assumptions of closed-system behaviour.

²⁷ In this contribution, we present partition coefficients for sodic clinopyrox-
²⁸ ene and silicate melts of tephriphonolite to phonolite composition, as deter-
²⁹ mined from internally heated pressure vessel experiments on synthetic and
³⁰ natural compositions. These are complemented by well-constrained natural
³¹ volcanic phenocryst-glass pairs from Canary Islands pyroclastic fall deposits.
³² We characterise the mineral compositional controls on element-partitioning
³³ behaviour and present a predictive model for clinopyroxene/melt element-
³⁴ partitioning that can be used to generate clinopyroxene/melt partition coef-
³⁵ ficients using only clinopyroxene major-element compositions (e.g., as mea-
³⁶ sured by electron-microprobe). This approach permits forward modelling of
³⁷ element budgets during differentiation processes in magmatic systems, in-
³⁸ cluding evolved sodic alkaline systems, as well as providing a mineral-based
³⁹ tool that can be used to reconstruct parental melt compositions from clinopy-
⁴⁰ roxene compositions in natural rocks.

⁴¹ 2. Methodology

⁴² 2.1. Experiment starting materials

⁴³ Clinopyroxene were synthesised in sodic alkaline melts of varying com-
⁴⁴ position to obtain a range of mineral compositions consistent with those in
⁴⁵ natural systems. Starting glass compositions are given in Table 1 and Fig-
⁴⁶ ure S1. Synthetic glasses L1 and L5 were prepared from reagent-grade oxide
⁴⁷ and carbonate powders, ground together in an agate mortar, decarbonated
⁴⁸ for 6 hr at 450°C, then homogenised in air for 3 hr at 1400°C in a Pt cru-
⁴⁹ cible. Repeated fusion and grinding in agate ensured chemical homogeneity

50 of the starting glasses, which was confirmed by electron-microprobe analyses
51 of the final fused glass. Finely ground Mud Tank zircon was added to the
52 homogeneous major-element glasses as a source of Zr, Hf, Nb and Ta; the
53 glasses were then fused for a further three hours at 1400°C. The remaining
54 trace-elements were added as a cocktail of single element nitrate solutions
55 (ICP-MS standards), dried onto the powdered glasses, then denitrified at
56 450°C for 30 minutes. The synthetic basanite L1 and phonolite L5 were
57 mixed in varying proportions to make the low alkali (L) series of starting
58 glasses, while dried NaOH and KOH powders were added to make the mid-
59 dle (M) and high (H) alkali starting glasses. Analyses of glass compositions
60 L5 and H5, quenched from superliquidus conditions, confirm that Henry's
61 law was respected (Supplement S1).

62 A well-mixed rock powder from the Nechalacho Layered Suite in Canada
63 (Möller and Williams-Jones, 2016, Unit NLS-9, sample L09-194-405.5, al-
64 ternative sample name VM 11-6) was used as experimental starting mate-
65 rial for a more extreme peralkaline composition. This composition was not
66 fused prior to loading into experiment capsules, so as to preserve the origi-
67 nal volatile element concentrations. An experiment using this material that
68 was quenched from superliquidus conditions is homogeneous with respect to
69 major-elements, as determined from EPMA measurements.

70 *2.2. Experimental equipment and procedures*

71 In total, 36 partitioning experiments were conducted in a Harwood-type
72 internally heated pressure vessel (IHPV) in the HP-GeoMatS laboratory at
73 the German GeoForschungsZentrum (Table S1). Temperature was measured
74 with Type-S thermocouples calibrated against the melting point of NaCl

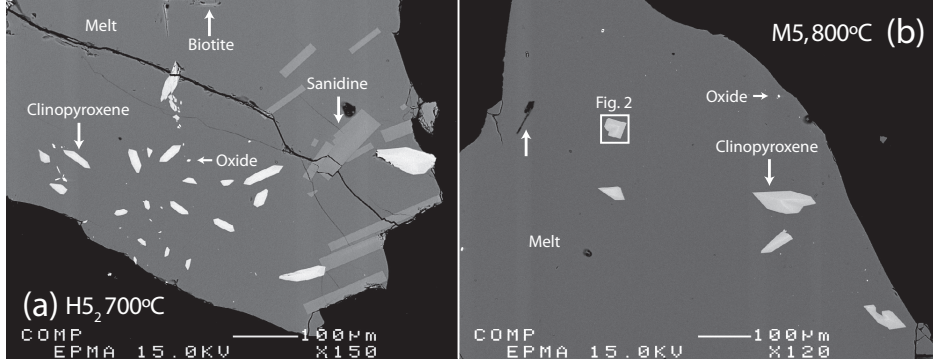


Figure 1: Backscattered electron images showing typical textures of run products from the internally heated pressure vessel experiments. Crystal fractions are typically small (<10% by area), with blade-shaped, euhedral clinopyroxene and glasses free of quench crystals.

(Borchert et al., 2010, accuracy of ± 5 °C at 200 MPa). Argon gas was used as the pressure medium, and pressure was measured with a strain gauge to an accuracy of ± 7 MPa. During the experiments, pressure was controlled automatically and held within ± 5 MPa of stated values.

Oxygen fugacity was buffered to the intrinsic redox conditions of the experimental setup, which corresponds to $\log f\text{O}_2 \text{ ca. } \Delta\text{QFM} + 1$ in our H_2O -saturated charges (see Chou, 1986; Berndt et al., 2002; Jugo et al., 2010). One experiment using the Nechalacho Layered Suite composition was performed in a double capsule with a haematite solid buffer, designed to increase $f\text{O}_2$ and promote crystallisation of Fe^{3+} -rich clinopyroxene (Eugster and Wones, 1962). This experiment ran at the Hm-Mt buffer, which corresponds to $\log f\text{O}_2 \approx \Delta\text{QFM} + 5$, as confirmed by presence of both buffer minerals in the outer capsule following quench. The experiments were designed to run between the liquidus and solidus for each composition, which corresponds to

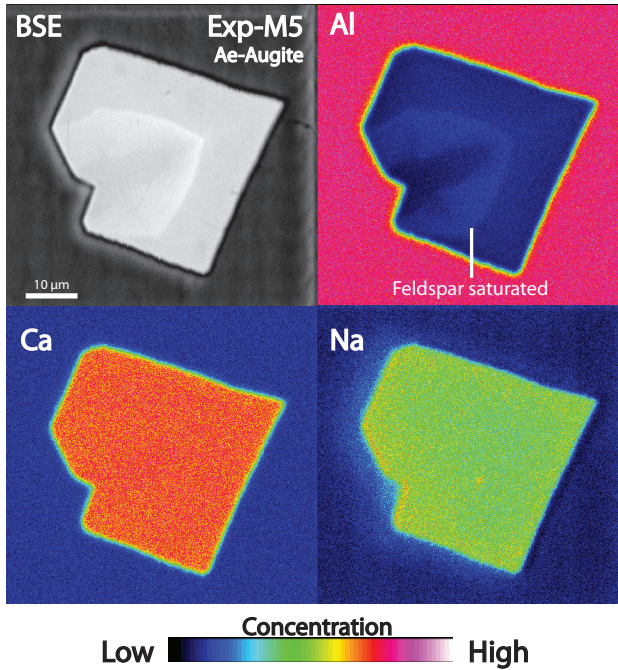


Figure 2: Element maps of clinopyroxene from internally heated pressure vessel experiment M5 (see box in lower magnification image, Fig. 1b). Aegirine-augite clinopyroxene have a sharp internal boundary that reflects feldspar saturation and are subtly zoned. Further element maps are available as an electronic supplement (Fig. S2).

89 temperatures between 650 and 825°C, all at 200 MPa pressure (Table S1).
 90 Powdered starting glass and distilled, deionised water were welded inside
 91 3 or 3.5 mm outer diameter platinum capsules of 20–25 mm length (see Ta-
 92 ble S1). To verify that capsules were sealed, they were heated to 110°C and
 93 weighed before and after. The amount of water sealed inside the capsules
 94 varied with temperature and composition and was kept in excess of sat-
 95 ration (Carroll and Blank, 1997; Moore et al., 1998; Schmidt and Behrens,
 96 2008). Water saturation was confirmed post-run by puncturing capsules and

97 checking for water expulsion and mass loss on drying at 110°C.

98 The capsules were loaded into the vessel, pressurised to 200 MPa, then
99 heated to superliquidus temperatures for at least 16 h (Table S1) to per-
100 mit homogenisation of trace-element concentrations, dissolution of water and
101 equilibration of fO_2 by exchange of H₂ through the capsule wall (cf. Gaillard
102 et al., 2002). Following homogenisation, temperature was lowered to run
103 conditions. An initial set of experiments were cooled rapidly from homogeni-
104 sation to run temperature at about 100°C/min. A second set of experiments
105 were cooled to run temperature at 1°C/min to promote slow growth of crys-
106 tals and to minimise the formation of compositional gradients in the melt.
107 Vessel temperature was then cycled between run temperature and run tem-
108 perature + 10°C to promote dissolution of small crystals at the expense of
109 larger grains, and to promote crystal growth close to the run temperature.
110 Element partitioning results are consistent among experiments of different
111 cooling paths. In all experiments, run temperature was kept constant for at
112 least 40 h to allow for chemical homogenisation of melt and growth of crystals
113 via Ostwald ripening. Capsules were then quenched to room temperature.

114 To minimise the growth of groundmass crystals on cooling, a rapid quench
115 apparatus was used where possible (Berndt et al., 2002, Table 2). We have
116 not measured quench rates in this vessel, but the capsules probably cooled
117 at rates in excess of 100°C/s. For the rest of the experiments, quenching
118 was achieved by cutting power to the furnace, which resulted in cooling to
119 below the glass-transition temperature (< 350°C; Giordano et al., 2005) in
120 less than 150 s.

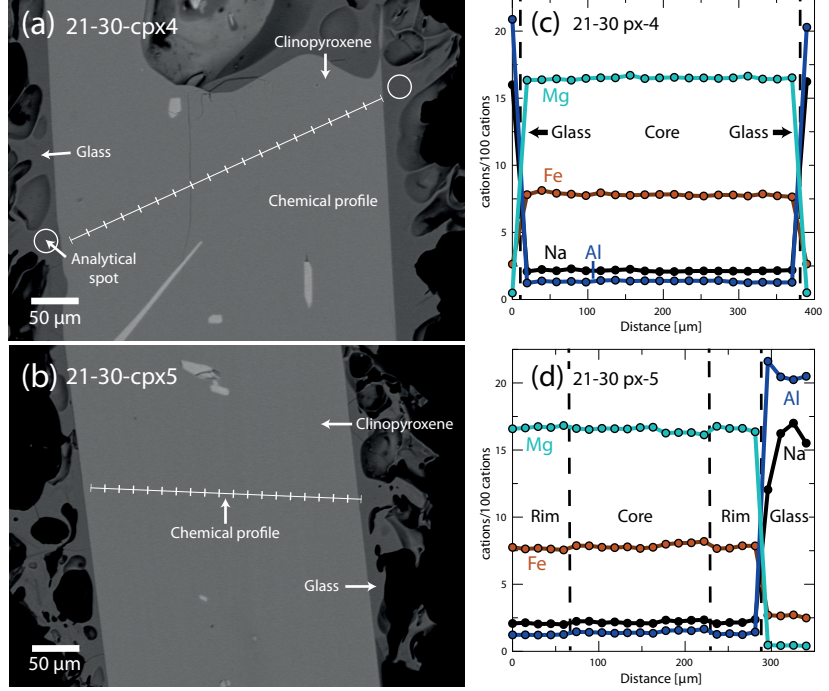


Figure 3: Examples of textural features from Canary Islands clinopyroxene phenocrysts from this study. (a, b) Backscattered electron images show that crystals are euhedral and are free from complex zoning patterns. (c, d) Chemical profiles across clinopyroxene phenocrysts and glass rims (quenched melt), as measured by wavelength dispersive spectroscopy, showing that zoning is effectively absent in these clinopyroxene. In (c) analyses of glass are aligned with the chemical profile shown in (a). Glass analyses shown in (d) are from rims of quenched melt from other clinopyroxene phenocrysts recovered from the same pumice sample. Both pictured phenocrysts are from the basal air fall deposit, associated with the ~2 ka eruption of Pico Viejo, Tenerife (Ablay et al., 1995).

121 *2.3. Natural samples*

122 Alkaline volcanism on Tenerife is associated with a weak thermal mantle
123 plume that impinges upon thick, old, slow-moving oceanic lithosphere (Car-

¹²⁴ racedo et al., 2007). This geological scenario has favoured development of a
¹²⁵ complex magma-plumbing system that produces a great diversity of volcanic
¹²⁶ products from alkali basalt to phonolite in composition. The Las Cañadas
¹²⁷ edifice, a large, central, composite stratovolcano (Bryan et al., 1998; Brown
¹²⁸ et al., 2003; Edgar et al., 2007), rests upon a base of at least three mafic al-
¹²⁹ kaline shield volcanoes (Thirlwall et al., 2000; Guillou et al., 2004; Gurenko
¹³⁰ et al., 2006). Xenoliths indicate that a nepheline syenite intrusive system
¹³¹ underlies the island (Wiesmaier et al., 2012).

¹³² Six clinopyroxene/glass pairs from four different volcanic eruptions on
¹³³ Tenerife have been investigated. The \sim 2 ka eruptive products of Montaña
¹³⁴ Blanca and Pico Viejo (Abhay et al., 1995) are phonolitic, plinian fall de-
¹³⁵ posits, whereas Montaña Samara is a monogenetic, mafic cinder cone (Albert
¹³⁶ et al., 2015). Phase-equilibrium experiments conducted on Montaña Blanca
¹³⁷ unit UMB-II suggest that magma was stored prior to eruption at $850 \pm 15^\circ\text{C}$,
¹³⁸ 50 ± 20 MPa, with 2.5 ± 0.5 wt% H₂O at $\log f\text{O}_2 \approx \text{NNO} - 0.5$ (Andújar and
¹³⁹ Scaillet, 2012). Field locations, mineral proportions and major-element com-
¹⁴⁰ positions of the clinopyroxene and glasses are presented in Table S1.

¹⁴¹ 2.4. Sample preparation

¹⁴² Experiment capsules were torn open with pliers, and charges were split
¹⁴³ using a low-speed wafering saw. Samples were mounted in epoxy resin and
¹⁴⁴ polished for *in situ* chemical analyses.

¹⁴⁵ Natural pyroclastic rocks were rinsed in tap water and crushed with a
¹⁴⁶ hammer. Crystals and glass fragments, hand-picked from a sieved size-
¹⁴⁷ fraction between 1.18 mm and 125 μm , were used to make grain mounts
¹⁴⁸ containing 5–20 crystals of clinopyroxene per sample. Natural samples also

¹⁴⁹ contain biotite, sanidine, ± spinel, amphibole, olivine, titanite and sodalite.
¹⁵⁰ Clinopyroxene mineral mounts were examined using backscattered electron
¹⁵¹ imaging to select euhedral crystals that were free from melt inclusions and
¹⁵² chemical zoning ($n = 6$, Fig. 3).

¹⁵³ **3. Analytical techniques**

¹⁵⁴ All experimental products were examined by reflected light optical mi-
¹⁵⁵ croscopy and SEM, and all phases produced were identified by electron-
¹⁵⁶ microprobe using an energy-dispersive detector. Images were obtained to
¹⁵⁷ estimate modal proportions of phases, which were calculated using ImageJ
¹⁵⁸ freeware (Rasband, 2016, see Table S1).

¹⁵⁹ *3.1. Electron-microprobe analysis*

¹⁶⁰ Major-element compositions of experimental products and natural min-
¹⁶¹ erals and glasses were measured with a JEOL 8900 instrument at McGill
¹⁶² University and a JEOL 8230 instrument at the University of Ottawa (Table
¹⁶³ 3). An accelerating voltage of 15 kV was used with a 15 nA beam of $5 \mu\text{m}$
¹⁶⁴ diameter for minerals, and a 4 nA beam of $50 \mu\text{m}$ diameter for glasses. Count
¹⁶⁵ times for all elements were 60 s. Using the above routine, we observed no
¹⁶⁶ sodium loss over the measurement time period. For the silicate minerals and
¹⁶⁷ glasses, both synthetic and natural minerals or oxides were used for calibra-
¹⁶⁸ tion (see Table S1). Analytical uncertainties were determined by multiple
¹⁶⁹ analyses of reference materials and duplicate analyses of samples.

¹⁷⁰ Element distribution maps were generated with a JEOL 8900 instrument
¹⁷¹ at McGill University using an accelerating voltage of 15 kV, a focussed 40
¹⁷² nA beam, and a dwell time of 50 ms per pixel (Figs. 2, S2). Fe, Ti, Al, Si

¹⁷³ and Na were measured with wavelength-dispersive detectors, while Ca and
¹⁷⁴ Mg were measured with an energy-dispersive spectrometer.

¹⁷⁵ Transects of Ce, Mg and Fe concentrations within the experiment clinopy-
¹⁷⁶ roxene were measured with a JEOL 8900 instrument at McGill University
¹⁷⁷ using a focussed beam of 50 nA with an accelerating voltage of 20 kV. Ce
¹⁷⁸ was counted with a wavelength-dispersive spectrometer with an LIFH crystal
¹⁷⁹ for 100 s (MAC-Ce standard). Mg and Fe were counted for 20 s, with TAP
¹⁸⁰ and LIF crystals respectively (diopside and olivine standards, respectively).
¹⁸¹ Matrix corrections for Mg, Fe and Ce were not possible with these data, for
¹⁸² lack of other major-elements measured, however their relative values may
¹⁸³ still be used to assess the extent to which the clinopyroxene are chemically
¹⁸⁴ zoned.

¹⁸⁵ *3.2. Laser-ablation ICP-MS*

¹⁸⁶ Trace-element concentrations of clinopyroxene and glasses were deter-
¹⁸⁷ mined by laser-ablation ICP mass-spectrometry. Analyses were performed
¹⁸⁸ at McGill University using a NewWave 213 nm Nd-YAG laser system coupled
¹⁸⁹ to a Thermo Finnigan iCAP-Qc quadrupole ICP-MS instrument. Typical flu-
¹⁹⁰ ence was 3–12 J/cm² (from 80 µm to 8 µm spot sizes), with a repetition rate
¹⁹¹ of 10 Hz. Ablated material was transferred to the ICP-MS in a He flow of 800
¹⁹² mL/min and mixed with Ar prior to injection into the plasma. Instrumental
¹⁹³ drift was monitored by repeat analyses of the primary standard glass BCR-
¹⁹⁴ 2G, with bias monitored by repeat analyses of secondary standards UTR-2
¹⁹⁵ peralkaline rhyolite and USGS-RGM-1 rhyolite glasses (Table S1). Sample
¹⁹⁶ surfaces were pre-ablated to remove residues from polishing materials and to
¹⁹⁷ improve ablation efficiency.

198 Primary and secondary standards and an unzoned Canary Islands clinopy-
199 roxene were analysed with beam sizes of 8–80 μm to monitor crater-size-
200 dependent element-fractionation effects; none were found for the elements
201 reported here. For minerals and glasses in the experimental charges, beam
202 sizes of 8–40 μm and 16–80 μm were used, respectively. Depending on grain-
203 size and availability, 5–14 mineral grains and 3–10 areas of glass were anal-
204 ysed per charge. Natural clinopyroxene and rim glasses were analysed using
205 a beam size of 12–80 μm and 12–30 μm , respectively. Wherever possible,
206 ablation was performed along lines parallel to crystal rims (1–3 $\mu\text{m} / \text{s}$).

207 Drift corrections and data reduction were conducted in Iolite v2.5 (Paton
208 et al., 2011). The total of major-elements measured by LA-ICP-MS or, where
209 available, the Al concentration from electron-microprobe analyses, was used
210 as an internal standard (Table 3). For some experiments, ablation through
211 the minerals was too rapid to generate a stable signal for data-reduction
212 purposes. In these cases, a mixing model was applied to estimate the com-
213 position of these clinopyroxene, similar to those applied by Rubatto and
214 Hermann (2007); Yang et al. (2018)(see supplementary methods S4).

215 4. Results

216 4.1. Run product phase stability and crystallinity

217 Trace-element partition-coefficients are reported for eleven experimental
218 charges. 25 additional experiments were rejected as their run temperatures
219 were superliquidus or subsolidus, or because their growth textures were in-
220 dicative of disequilibrium (e.g. Fig. S2). Phase proportions are provided in
221 Table S1.

222 All reported experimental runs were near-liquidus (3–22% crystals, RL
223 images) and are characterised by a homogeneous distribution of phases (Fig
224 1), except for experiments H5₃ and NLS-9_{2-HM}, in which sanidine crystals
225 are concentrated at the centre. Glasses are clean, homogeneous and show a
226 limited range of major- and trace-element compositions for each experiment
227 (Fig. S1). Clinopyroxene crystals are generally small, euhedral blades with
228 a narrow range of sizes for a given experiment (<10 µm to 100 µm in cross
229 section, Figs. 1–2). In addition to clinopyroxene and glass, experiments on
230 mafic to intermediate compositions produced magnetite, titanite ± kaersu-
231 tite amphibole, whereas some phonolitic experiments produced biotite, alkali
232 feldspar ± magnetite (Table S1).

233 Constraining the full phase equilibria of all of the investigated composi-
234 tions was beyond the scope of this study. Run conditions and run products
235 given in Supplement S1 provide insight into phase equilibria that might guide
236 future studies. In our experiments it can be seen that clinopyroxene has a
237 wide stability field across the investigated physicochemical conditions, with
238 only a single starting composition generating amphibole in place of pyroxene
239 (experiments L3 and L3₂).

240 *4.2. Glass compositions*

241 All run-product glasses are homogeneous across the length and breadth
242 of the experiment capsules based on multiple electron-microprobe and laser-
243 ablation ICP-MS analyses. Most major-element oxide compositions, as mea-
244 sured by electron-microprobe, show relative standard deviations of < 5%
245 within experiment capsules, with minor-elements oxides (concentration <
246 1%) showing greater variability, most with standard deviations between 5

and 10 % relative. Trace-element compositions of the glass, as measured by laser-ablation ICP-MS, typically show time-weighted relative standard deviations of 1 to 8% within each capsule, with this variability depending on both the absolute concentration of that element and on the beam-size that was used for analyses (Supplement S1). Low sum-totals of major-element oxide concentrations in the electron microprobe analyses are a result of high dissolved water contents in the quenched melt.

On a total-alkalies vs. silica diagram the experiment glasses are predominantly phonolitic in composition, though span the trachyte-phonolite join (Fig. S1). Their alkalinity index (molar $(\text{Na} + \text{K})/\text{Al}$) is 0.85 to 1.40, spanning the alkaline–peralkaline join and the Mg# of these quenched melts is 0 (Mg-free) to 22. The dissolved water content of these quenched melts is 8.8 to 10.7 wt.% (by difference method from EPMA data, with the Fe oxidation state assigned following Kress and Carmichael 1991) and their NBO/T ratios are 0.98 to 1.42 (Mysen et al., 1982, 1985). The halogen content of the synthetic experiments is nominally zero, whereas glasses from the Nechalacho Layered Suite composition experiments typically contain 0.1 % F and 0.02 % Cl by weight.

The Canary Islands glasses are trachytic to phonolitic (CHECK) and are alkaline to weakly peralkaline in composition (alkalinity index of 0.78 to 1.16) with Mg# of 8 to 39. Dissolved water content and NBO/T ratios are not reported for these glasses because of post-eruptive loss of volatiles. These Canary Islands glasses typically contain 0.2 % F and 0.4 % Cl by weight.

To add: a more comprehensive figure showing glass compositions. This could be in the main text, or as a supplement

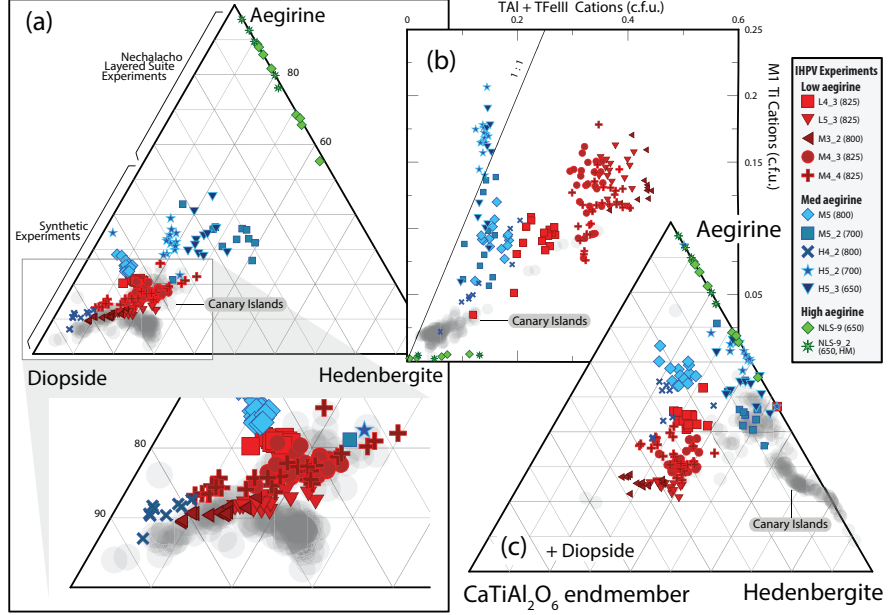


Figure 4: Clinopyroxene grown in internally heated pressure vessel experiments (a) expressed in terms of diopside, hedenbergite and aegirine end-members, (b) their M1Ti and tetrahedral Al and Fe³⁺ contents, and (c) expressed in terms of aegirine, hedenbergite and the theoretical CaTiAl₂O₆ end-member (Akasaka and Onuma, 1980). Clinopyroxene compositions from Canary Islands volcanic rocks are shown for comparison (this study). Fe²⁺/Fe³⁺ within the clinopyroxene was assigned following Droop (1987), then site occupancies and end-member proportions were allocated following Morimoto (1989). For methods used in calculation of the end-member proportions see Supplement S5. The range of clinopyroxene compositions within each experiment records changes to the composition of the melt during crystal growth, whereby the cores of the crystals record the first stage of crystallisation and the rims (highest Fe, Na) are in equilibrium with the quenched melt. **to finish! Also re-plot with a separate symbol to signify Canaries compositions that were used for the derivation of partition coefficients**

272 4.3. Compositions of the clinopyroxene and major-element exchange

273 The Canary Islands clinopyroxene are diopside (Di_{60-90} , Ae_{3-20} CHECK)
274 in composition, with most crystals containing about 0.05 c.f.u. ${}^{\text{IV}}\text{Al}$ (in the
275 T site) and 0.02 c.f.u. ${}^{\text{VI}}\text{Ti}$ (in the M1 site, Tables 3 and S1, Fig. 4). Ex-
276 periments on the synthetic compositions produced clinopyroxene of diopside
277 to aegirine-augite composition, a subset of which overlap with the compo-
278 sitional space defined by the Canary Islands clinopyroxene on a diopside–
279 hedenbergite–aegirine ternary diagram (Fig. 4a). This low-aegirine group
280 of synthetic clinopyroxene display a positive correlation between ${}^{\text{IV}}\text{Al}$ and
281 ${}^{\text{VI}}\text{Ti}$ content (red, *low aegirine*, Ae_{5-25}), and notably contain both of these
282 elements at elevated concentration relative to the Canary Islands clinopy-
283 roxene (${}^{\text{IV}}\text{Al} = 0.20\text{--}0.45$ c.f.u., ${}^{\text{VI}}\text{Ti} = 0.07\text{--}0.17$ c.f.u.). A further subset
284 of synthetic clinopyroxene have higher aegirine content (blue, *med aegirine*,
285 Ae_{25-50}) and show a similar range of Ti content to the low aegirine synthetic
286 minerals (0.05–0.18 c.f.u.), but a limited range of lower ${}^{\text{IV}}\text{Al}$ content (0.1–0.2
287 c.f.u., Fig. 4b). Experiments performed on the Nechalacho Layered Suite
288 composition (NLS-9, NLS-9_{2-HM}, green, *high aegirine*, Ae_{55-95}) reproduced
289 the aegirine-augite to aegirine clinopyroxene from the natural system (Möller
290 and Williams-Jones, 2016) that contain low concentrations of ${}^{\text{IV}}\text{Al}$ (up to 0.14
291 c.f.u.) and almost no ${}^{\text{VI}}\text{Ti}$, Ca or Mg.

292 The Canary Islands clinopyroxene that were selected for determination
293 of mineral–melt partition coefficients are free from melt inclusions, suggest-
294 ing relatively slow rates of crystal growth (Kennedy et al., 1993, Fig. 3).
295 Chemical zonation, if present, is of a similar magnitude to the analytical
296 precision of our electron microprobe, indicating that pressure, temperature

and melt composition remained stable during crystal growth. In the case of these Canary Islands clinopyroxene, the entire mineral is interpreted to be in chemical equilibrium with the adhered quenched melt. Trace-element abundances within these Canary Islands clinopyroxene show core-to-rim variations of about 1–5 % relative, with larger variations in element abundance associated with sector zoning than with concentric growth zoning (Supplement S1). (TO CONFIRM with images)

By contrast our experiment clinopyroxene display systematic compositional variation between their cores and rims; this variation recording changes to melt composition during growth of these crystals (e.g. Fig. 2). The systematics of crystal-chemical zonation both within individual experimental charges and within groups of experiments reveal major-element exchange vectors between the clinopyroxene and the melt. Three major-element exchange mechanisms correspond to the low (Ae_{5-25}), medium (Ae_{25-50}) and high (Ae_{55-95}) aegirine domains defined above (Figs. 4b, 5 and S3).

And may be used to infer.... the composition of the mineral assemblage that is crystallising? To discuss. Comments, please!

With increasing alkali content, the Si content in clinopyroxene increases at the expense of tetrahedrally co-ordinated Al and Fe^{3+} . As aegirine content increases, substitutions at the tetrahedral site become relatively less important than exchanges at the M1 and M2 sites. At the M1 site, the substitution of Ti for ions of 2+ and 3+ valence correlates well with the exchange of tetrahedrally coordinated 3+ cations for Si^{4+} . The exchange behaviour of 2+ and 3+ cations at the M1 site depends on the aegirine content of the clinopyroxene. In low-aegirine clinopyroxene, the concentration of 3+ ions at the

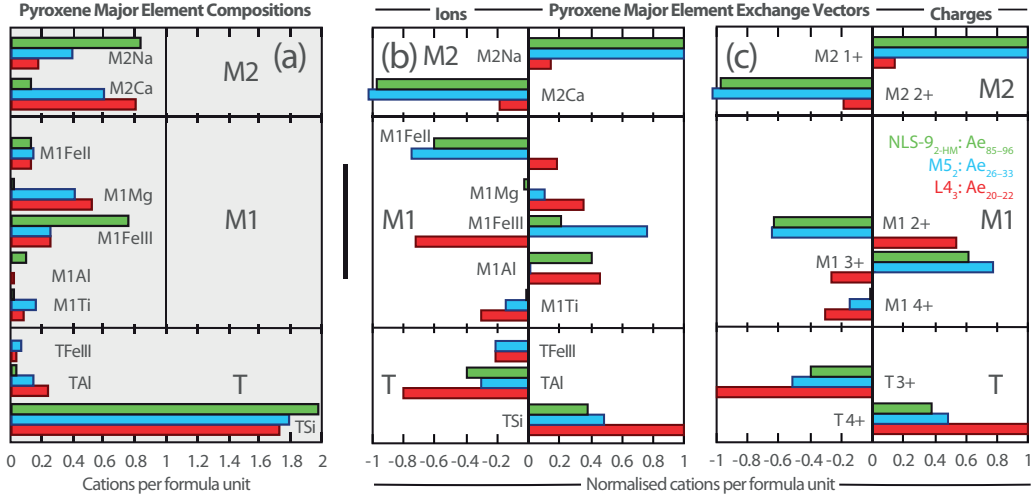


Figure 5: Bar charts showing clinopyroxene composition and major-element exchange mechanisms for three experiments representative of high (green), medium (blue) and low-aegirine (red) clinopyroxene. (a) clinopyroxene major-element compositions are expressed as cations per six-oxygen formula unit (b) exchange mechanisms grouped by ions, (c) grouped by charges. Methods used to calculate these exchange mechanisms are available in the caption of Supplementary Figure S3.

M1 site is negatively correlated with X_{Na}^{M2} , whereas in medium- and high-aegirine clinopyroxene, the M1 site takes progressively more 3+ ions as X_{Na}^{M2} increases. Substitutions of Ca^{M2} for Na^{M2} are relatively unimportant in low-aegirine clinopyroxene, but play a large role in medium- and high-aegirine exchange vectors.

Suites of Canary Islands clinopyroxene follow similar major-element exchange systematics to our low aegirine experiment clinopyroxenes (CHECK, expand if necessary).

330 4.4. Trace-element concentrations in the experiment clinopyroxene

331 Assessing the homogeneity of trace-element concentrations within miner-
332 als is important when defining their equilibrium partition-coefficients because
333 only the rims record true chemical equilibrium with the adjacent melt. Mea-
334 surements of trace-element concentrations in experimentally-grown minerals
335 are often challenging as a result of their small size; They are commonly com-
336 parable in scale to the beam-size of laser-ablation or SIMS systems ($\sim 10-20$
337 μm). In many cases it is therefore not possible to assess the extent to which
338 trace-element concentrations are zoned within experimentally-grown crystals.
339 To assess the extent to which trace-element concentrations are zoned within
340 our experiment clinopyroxene, electron-microprobe transects were measured
341 across seven crystals for the elements Mg, Fe and Ce (Supplement S3). Tran-
342 sects were made across grains from three experiments, each crystallised to
343 varying degrees.

344 The transects reveal that clinopyroxene Ce-concentration follows both
345 sector-zoning and concentric growth-zoning patterns, as recorded by backscat-
346 tered electron images and the $X\text{Mg}$ of the clinopyroxene. Sector-zoning has
347 a more pronounced effect on the Ce-concentration in the clinopyroxene than
348 concentric growth-zoning, causing one transect to appear ‘laterally-zoned’
349 and another to appear ‘reverse-zoned’ in terms of Ce-concentration. These
350 effects are due to sector-zoning, with bright sector-zones on BSE images as-
351 sociated with higher Ce-concentrations than dark zones. To gain insight into
352 the variation in clinopyroxene Ce-concentration associated with concentric
353 growth-zoning, analyses were grouped *per-experiment* to average this sector-
354 zoning effect. Ratios of median average Ce-counts / rim Ce-counts represent

355 the difference between the composition of the bulk crystal, as analysed by
356 LA-ICP-MS, and the composition of the clinopyroxene rims that approach
357 chemical equilibrium with the adjacent quenched melt and have a mean value
358 of 1.08, ranging between 1.04 and 1.12. The highest values are found for the
359 largest clinopyroxene crystals and in these, because of their size, we were
360 able to avoid the cores in the analyses via LA-ICP-MS, reducing the growth-
361 zonation bias in trace-element partition-coefficients.

362 Where large clinopyroxene crystals were present and time-averages of el-
363 ement counts could be used for the reduction of laser-ablation data, trace-
364 element compositions are similar among clinopyroxene crystals within indi-
365 vidual experiments (Fig. TO ADD??) indicating that trace-element con-
366 centrations in the melt phase remained spatially homogeneous throughout
367 the duration of the experiments. Typical trace-element concentrations in the
368 experiment clinopyroxene are illustrated in Supplementary Figure S4c.

369 5. Discussion

370 5.1. Attainment of equilibrium in the Canary Islands rocks

371 The Canary Islands trace-element partition-coefficients presented here
372 were determined from euhedral, blade-shaped crystals free of melt inclu-
373 sions and chemical zonation. The corresponding quenched melt was in direct
374 contact with these crystals and shows no zonation in backscattered electron
375 images (Fig. 3). While equilibrium conditions are challenging to confirm for
376 a natural volcanic system, the euhedral forms, chemical homogeneity of crys-
377 tals, and congruency between samples from separate eruptions suggest that
378 the crystals grew in a stable environment, and were not subject to chemical

³⁷⁹ or physical perturbations during growth (Fig. 6).

³⁸⁰ *5.2. Attainment of equilibrium in the experiments*

³⁸¹ Experiments used to determine trace-element-partition coefficients must
³⁸² have attained, or at least closely approached, chemical equilibrium. Un-
³⁸³ fortunately no experiments are able to determine equilibrium trace-element
³⁸⁴ partition-coefficients *sensu stricto* because reversal experiments, where a
³⁸⁵ clinopyroxene re-equilibrates with a melt, are not possible owing to sluggish
³⁸⁶ diffusion of most elements through the clinopyroxene structure (Van Orman
³⁸⁷ et al., 2001; Zhang et al., 2010). The following two sections discuss some an-
³⁸⁸ alytical and experimental biases that must be considered when determining
³⁸⁹ trace-element partition-coefficients from crystallisation experiments.

³⁹⁰ *5.2.1. The formation of diffusive boundary layers*

³⁹¹ A potential barrier to chemical equilibration during crystallisation is the
³⁹² formation of a diffusive boundary layer within the melt adjacent to growing
³⁹³ crystals. In a perfect equilibrium case there are no compositional gradients
³⁹⁴ in the melt at any time during crystal growth. However in reality the growth
³⁹⁵ of crystals depletes compatible elements from the melt and residually en-
³⁹⁶ riches incompatible elements. Theoretically, this process of crystal growth
³⁹⁷ results in formation of a (potentially ephemeral) diffusive boundary layer in
³⁹⁸ the melt directly adjacent to the crystal that is depleted with respect to
³⁹⁹ compatible elements and enriched with respect to those that are incompat-
⁴⁰⁰ ible (Lu et al., 1995). The composition of such a diffusive boundary layer
⁴⁰¹ depends on both the relative enrichment or depletion of elements during the
⁴⁰² crystallisation process, and the rate at which these elements diffuse through

403 the melt. Rapidly-diffusing elements with partition-coefficients close to unity
404 will have concentrations closest to that of the bulk melt.

405 Experiments designed to investigate trace-element-partitioning behaviour
406 might employ slow cooling rates to limit the development of diffusive bound-
407 ary layers, thus forming crystals from melt that is closer in composition to
408 that of the bulk experiment. Such experiments then run into another prob-
409 lem, in that significant crystallisation may occur at temperatures above that
410 of the final run temperature. Rapidly-cooled experiments circumnavigate
411 this issue, but may form relatively more pronounced diffusive boundary layers
412 during crystal growth that become ‘flattened out’ during the homogenisation
413 stage of the experiment.

414 Numerous diffusion data have been gathered for silicate melts over the
415 past few decades, and a comprehensive review is given by Zhang et al.
416 (2010). Diffusion of trace-elements through water-saturated peralkaline melts
417 is rapid, owing to their depolymerised structure. For example Lanthanum
418 diffusion-coefficients are 6 orders of magnitude higher than for water-saturated
419 granitic compositions of a similar temperature (compare Rapp and Watson,
420 1986; Behrens and Hahn, 2009). This rapid diffusion serves to minimise the
421 formation of diffusive boundary layers adjacent to growing crystals in our
422 experiments. Coupled diffusion mechanisms complicate the application of
423 measured single-element diffusion-coefficients to a crystallising system (Grove
424 et al., 1984; Liang et al., 1994; Costa et al., 2003). Here, the diffusive flux of
425 trace-elements may be coupled to gradients in major-element concentration
426 within the melt.

427 To investigate the impact of diffusive effects on trace-element-partitioning

428 between clinopyroxene and melt, Mollo et al. (2013) performed crystallisa-
429 tion experiments on trachybasaltic melts at a range of cooling rates (2.5–
430 50°C / hr). Rapid cooling rates result in depletions of Si, Ca and Mg in
431 the clinopyroxene that are compensated for by enrichments in Al, Na and
432 Ti. Regardless of cooling rate, Ounma parabolae could be fitted through
433 isovalent sets of partition coefficients, indicating that crystal-lattice-effects
434 dominated over those associated with the formation of diffusive boundary
435 layers and that local equilibrium was achieved at the time of crystallisa-
436 tion. In their rapidly-cooled experiments, Mollo et al. (2013) found apparent
437 clinopyroxene/melt trace-element-partition coefficients that varied with iden-
438 tical crystal-chemical systematics to true equilibrium partition coefficients,
439 the magnitude of both sets of trace-element-partition-coefficients following
440 the ^{IV}Al content of the clinopyroxene (*ibid.*, their Fig. 9). Deviations of
441 the partition coefficient of several orders of magnitude can be obtained only
442 when rapidly growing crystals entrap small portions of the diffusive boundary
443 layer that are found as minute melt inclusions randomly distributed in the
444 mineral phase (Kennedy et al., 1993). In this extreme case, partitioning be-
445 haviour is obviously influenced by contamination phenomena and no Onuma
446 parabolae can be derived. As Onuma parabolae could successfully be fitted
447 through partitioning data for all of our presented experiments (see following
448 sections), and no melt inclusions were observed in optical and electron imag-
449 ing, we infer that our data were not affected by the presence of such melt
450 inclusions, and that they may be compared directly with partitioning data
451 derived from experiments that employed slower cooling rates.

452 5.2.2. *Chemical zonation in the experiment clinopyroxene: Theoretical frame-*
453 *work*

454 Trace-elements diffuse slowly through the clinopyroxene structure relative
455 to that of the melt (Van Orman et al., 2001; Zhang et al., 2010), therefore no
456 re-equilibration of trace-elements takes place on an experimental time scale.
457 Strictly speaking, clinopyroxene only record true equilibrium conditions at
458 their outermost rim. Experiments designed for the derivation of equilibrium
459 partition coefficients ideally minimise bias by limiting the fraction of crystalli-
460 sation, producing minerals that are as homogeneous as possible. Currently
461 available *in situ* analytical techniques for trace-element abundances, such as
462 LA-ICP-MS and SIMS, are limited in terms of minimum beam-size to \sim 10
463 μm ; chemical zonation, however subtle, will be continuous from the core to
464 the rim of the mineral. Consequently, no experimentally derived partition
465 coefficients record equilibrium partition coefficients *sensu stricto*, but when
466 properly conducted, may closely approximate chemical equilibrium.

467 Because only the very rim of a crystal records chemical equilibrium with
468 the adjacent melt, and some internal portions of the minerals must be sam-
469 pled during *in-situ* analyses all experimentally-determined trace-element partition-
470 coefficients are biased toward higher values for compatible elements and lower
471 values for incompatible elements. The magnitude of these biases depend
472 on the fraction of crystallisation in the experiment, the true equilibrium
473 partition-coefficient of that element, as well as the proportion of each growth-
474 zone sampled during the *in-situ* analysis. Fortunately *in-situ* chemical anal-
475 yses preferentially sample the mantle and rim of zoned crystals because few
476 analyses section a crystal perfectly through the core. As a result there is a

477 sampling bias toward equilibrium mineral compositions.

478 Consider a hypothetical experimental system in which 20% of the melt
479 crystallises as a single mineral, and where the chemical analyses of that
480 mineral are truly bulk averages of that mineral composition. An incompatible
481 element with a true equilibrium partition coefficient of 0.1 would return a
482 measured partition coefficient of 0.09, a small bias because the concentration
483 of that incompatible element in the melt changed only subtly during the
484 course of crystallisation. For compatible elements with true D_i values of
485 ~ 10 , measured partition coefficients can be a factor of 2–3 higher than true
486 partition coefficients, because their concentration in the melt changes more
487 than an incompatible element during the course of crystallisation.

488 Further complexity is introduced in systems that crystallise multiple min-
489 erals simultaneously. In the case of experiment M3₂, the REE are compatible
490 in clinopyroxene, but are incompatible in biotite and oxides (e.g. Mahood and
491 Stimac, 1990; Schmidt et al., 1999). The REE have therefore been residually
492 enriched in the melt phase by the crystallisation of biotite and oxide miner-
493 als, while simultaneously being depleted from the melt by crystallisation of
494 clinopyroxene. These two competing processes serve to minimise the effect of
495 fractional crystallisation on the concentration of trace-elements in the melt
496 and consequently derived REE partition-coefficients between clinopyroxene
497 and melt will be closer to true equilibrium values.

498 5.2.3. *Implications of the cerium zonation across the experiment clinopyrox-
499 ene*

500 Because of beam-size limitations and the small minerals generated in
501 the majority of our experiments it was not possible to measure all trace-

502 element concentrations within the core and rim of experiment clinopyroxene
503 separately. Electron-microprobe analyses offer smaller beam-sizes than LA-
504 ICP-MS systems, at the expense of precision and of number of elements.
505 This higher spatial resolution permitted investigation of the zonation of Ce
506 concentrations within the experiment clinopyroxene, with Ce as a proxy for
507 the other compatible elements.

508 The magnitude of concentric growth zoning in the experiment clinopy-
509 roxene was examined by averaging bulk and rim compositions across mul-
510 tiple sector-zoned grains within each experiment. The median Ce counts
511 divided by the rim Ce counts was 1.04 for experiment M3₂, 1.08 for exper-
512 iment M5 and 1.12 for fluorine-bearing experiment M3-1.25F (see Beard,
513 2018). Contrary to theory discussed above, the subtly (3%) crystallised
514 experiment M5 shows a greater variation in core to rim Ce content than
515 the more heavily (?? TO ADD%) crystallised experiment M3₂. Further-
516 more, the $D_{Ce}^{cpx/melt}$ for experiment M3₂ (6.2) is approximately double that
517 for experiment M5 (see discussion below), which should further promote the
518 formation of Cerium zonation in the clinopyroxene during crystallisation.
519 Consequently it is possible that many existing experimentally-derived trace-
520 element partition-coefficients are systematically offset from true equilibrium
521 values.

522 If Cerium is used as a proxy for the behaviour of compatible elements
523 in our experimental system, then apparent partition coefficients derived for
524 these elements via LA-ICP-MS are systematically offset to higher values by 4–
525 8%. Such a systematic bias is small, relative to the variation in clinopyroxene-
526 melt partition coefficients within our sample set, as well as in the literature.

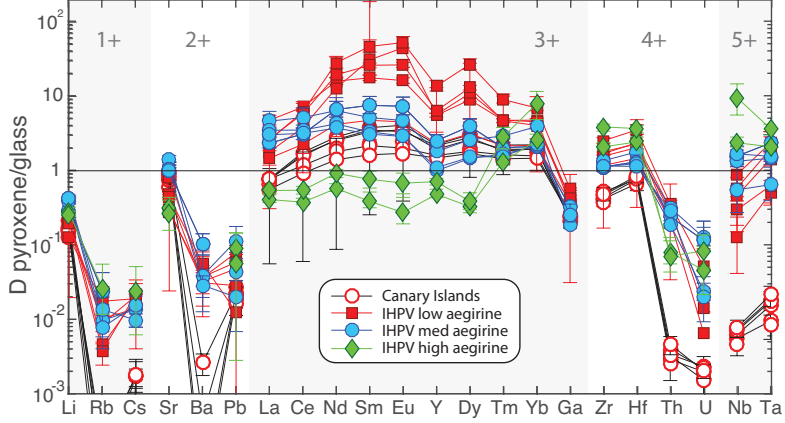


Figure 6: Trace-element-partition coefficients between clinopyroxene and melts, as determined from internally heated pressure vessel experiments ($n = 11$) and from clinopyroxene-rim glass pairs from pyroclastic fall deposits from Tenerife, Canary Islands ($n = 6$). Uncertainties on the partition coefficients are 1σ .

527 The effect of crystal zonation on incompatible element concentrations was
 528 not measured, but as outlined in the theoretical framework above, should
 529 be smaller than that for compatible elements. No correction factor has been
 530 applied to the data presented in the figures below, or in Tables 4 and S1.

531 *5.3. Trace-element-partitioning*

532 Element-partition coefficients and their uncertainties are reported in Ta-
 533 bles 4 and S1. Uncertainty calculations are described in the caption for Figure
 534 S4. Three markedly different behaviours of rare earth element-partitioning
 535 are observed in the experiments and Canary Islands rocks (Fig. 6). These de-
 536 pend on the aegirine concentration in the clinopyroxene and match the major-
 537 element exchange vector domains discussed above. Low-aegirine clinopyrox-
 538 ene (Ae_{5--25}), including those from the Canary Islands , prefer the MREE;

medium-aegirine clinopyroxene (Ae_{25--50}) show a similar behaviour, save for higher LREE partition coefficients, whereas high-aegirine clinopyroxene (Ae_{55--95}) strongly prefer HREE and show incompatible behaviour for the light and middle REE. The REE partition coefficients are 0.3–53, typically 2–6, with minima for LREE and MREE in high-aegirine clinopyroxene (Fig. 6). Our experimental partition coefficients are about an order of magnitude higher than in most other studies of clinopyroxene-melt element-partitioning that were performed on different bulk compositions (Fig. 7d,e,f), with the exception of high Si systems, such as the Bandelier Tuff (cf. Olin and Wolff, 2010). Canary Islands clinopyroxene have absolute REE partition coefficients about one order of magnitude lower than our low-aegirine experimental clinopyroxene.

The high field-strength elements (HFSE) Zr, Hf, Nb and Ta are compatible to slightly incompatible in the experimental clinopyroxene, and typically 1–2 orders of magnitude less compatible in the Canary Islands clinopyroxene (Fig. 7a,b,c). The HFSE are most compatible in sodic clinopyroxene. Partition coefficients for the large-ion lithophile elements K, Sr, Pb are positively correlated with X_{Na}^{M2} in the low- and medium-aegirine clinopyroxene, but are lower in high-aegirine clinopyroxene (Fig. S5). The Rb, Cs and Ba partition coefficients have a high uncertainty and are maximum estimates owing to low concentrations of these elements in the clinopyroxene, close to the detection limit for analyses by LA-ICP-MS. These data are therefore not discussed further. Lithium is incompatible ($D_{\text{Li}} = 0.1\text{--}0.4$) in both Canary Islands and experimental clinopyroxene and, like Sr and Pb, becomes more compatible with increasing aegirine content in the clinopyroxene, plateauing

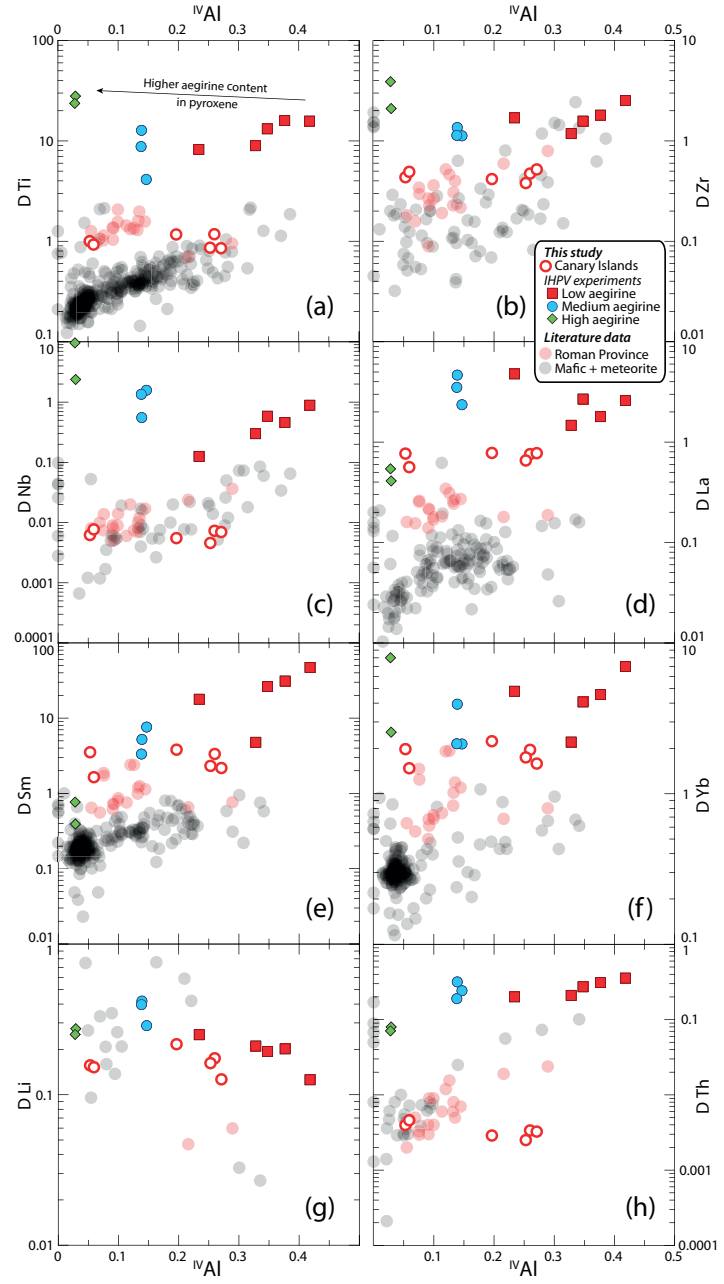


Figure 7: Element partition coefficients for HFSE (Ti, Zr, Nb), REE (La, Sm, Yb) and TE (Li, Th) vs. ^{IV}Al . Literature values ($n = 411$), including those from the Roman Province, Italy, are from the compilation of Bédard (2014), with additional, more recent, data from Mollo et al. (2016). A similar diagram with X_{Na}^{M2} in place of ^{IV}Al is in Supplement S5.

564 at $X_{Na}^{M2} = 0.4$ and decreasing thereafter (Figs. 7g, S5g). The actinides U
565 and Th show contrasting partitioning behaviour; the former showing no cor-
566 relation with aegirine content in the clinopyroxene, the latter becoming more
567 incompatible with increasing aegirine content (Fig. 7h). The U and Th par-
568 tition coefficients for our Canary Islands samples are similar to those for the
569 Roman Province (Wood and Trigila, 2001; Fedele et al., 2009; Mollo et al.,
570 2013, 2016), and are 1–2 orders of magnitude more incompatible relative to
571 the experimental clinopyroxene.

572 *5.4. Fits to the lattice-strain model*

573 The equilibrium partitioning of trace-elements between minerals and melts
574 is largely controlled by the structure of the crystal lattice, its elasticity (On-
575 uma et al., 1968; Kumazawa, 1969; Weidner and Vaughan, 1982) and its
576 ability to accommodate an excess or shortage in charge (Blundy et al., 1998;
577 Wood and Blundy, 2001; Hanchar et al., 2001; Corgne and Wood, 2005). The
578 lattice-strain model provides a framework in which the influence of these vari-
579 ables on partitioning behaviour can be quantified, and thus predicted under
580 conditions bracketed by a calibrating data set (Onuma et al., 1968; Blundy
581 and Wood, 1994; Wood and Blundy, 2014). Lattice structure has a depen-
582 dence on pressure, temperature and composition, and element-partitioning
583 is a thermodynamically controlled process (e.g. Wood and Blundy, 1997).

584 Most trivalent ions, including the REE and Y enter the larger M2 site
585 of clinopyroxene, which is typically 6- or 8-coordinated (Deer et al., 1992).
586 Smaller trivalent ions, including Al, Cr, Ga, Sc, and in the case of Fe-rich
587 clinopyroxene the HREE may enter the smaller, octahedral M1 site (Olin
588 and Wolff, 2010; Bédard, 2014). The high field-strength elements Ti, Zr, Hf,

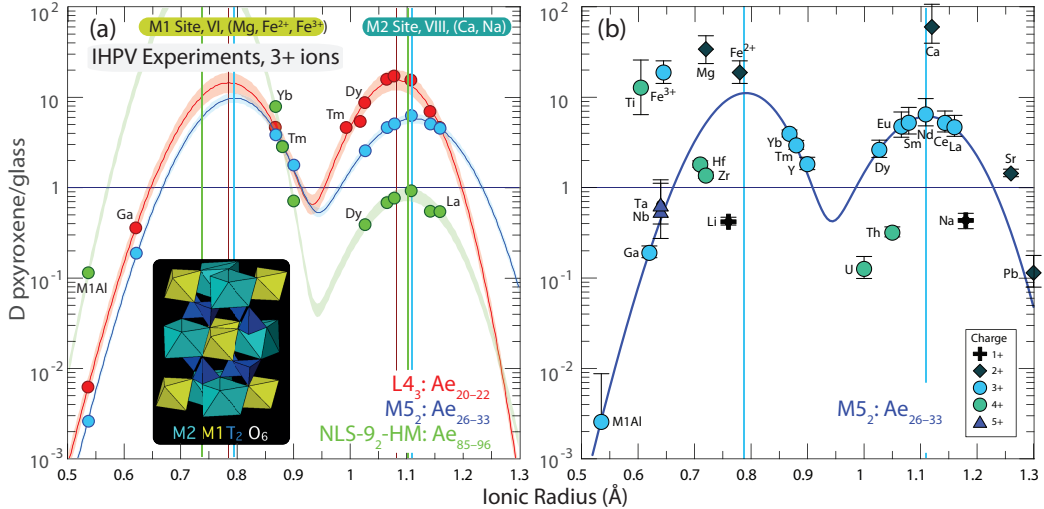


Figure 8: Non-linear weighted least-squares fits to element-partitioning data from the internally heated pressure vessel experiments following the lattice-strain model of Blundy and Wood (1994). (a) Representative fits to 3+ ion partitioning behaviour with examples for low (red), medium (blue) and high-aegirine (green) clinopyroxene experiments. (b) Measured partition coefficients for ions of 1+, 2+, 4+ and 5+ charges that are consistent with the lattice-strain model. Ionic radii are assigned to 6 or 8 fold co-ordination (Shannon, 1976), and were chosen to minimise residuals in the fit (cf. Olin and Wolff, 2010). Y was not included in the fitting routine for 3+ ions because of mass fractionation effects (ibid.). Vertical coloured lines indicate ideal ionic radii (r_0) of M1 and M2 sites and shaded areas indicate 95% confidence intervals on the fits determined via bootstrapping. Uncertainties on the partition coefficients in (b) are 1σ . Fitted lattice-strain parameters are given in Table 4.

589 Nb and Ta are typically hosted by the M1 site (Hill et al., 2000, 2011; Dygert
590 et al., 2014).

591 To investigate systematics in D_i values and the mechanisms by which
592 trace-elements are incorporated into clinopyroxene, element-partitioning be-

593 behaviour was explored in light of the lattice-strain theory, quantitatively de-
 594 scribed by the lattice-strain equation:

$$D_i^{mineral/melt} = D_0 \exp \left[\frac{-4\pi E_s N_a}{RT} \left(\frac{r_0}{2} (r_0 - r_i)^2 - \frac{1}{3} (r_0 - r_i)^3 \right) \right] \quad (1)$$

595 where r_0 is the ideal radius for the lattice site, E_s is the Young's modulus
 596 (i.e., the lattice site stiffness), D_0 is the strain-free partition coefficient, N_a is
 597 Avagadro's number, R is the gas constant, T is temperature in Kelvin, and
 598 r_i is the ionic radius of the element in question, all radii in Å. We focused on
 599 3+ ions that cover a wide range of radii and fitted lattice-strain parameters
 600 for both the M1 and M2 sites of clinopyroxene (Fig. 8):

$$D_i^{cpx/melt} = D_0^{M2} \exp \left[\frac{-4\pi E_s^{M2} N_a}{RT} \left(\frac{r_0^{M2}}{2} (r_0^{M2} - r_i)^2 - \frac{1}{3} (r_0^{M2} - r_i)^3 \right) \right] + D_0^{M1} \exp \left[\frac{-4\pi E_s^{M1} N_a}{RT} \left(\frac{r_0^{M1}}{2} (r_0^{M1} - r_i)^2 - \frac{1}{3} (r_0^{M1} - r_i)^3 \right) \right] \quad (2)$$

601 Parabolae for 3+ ions were fitted for the M1 and M2 sites using the
 602 REE, Ga and Al assigned to the M1 site of clinopyroxene (Fig. 8a). Fits are
 603 weighted based on uncertainties for the element-partition coefficients. HREE
 604 have higher element-partition coefficients than can predicted by substitution
 605 into the M2 site, hence were fitted with ionic radii for sixfold coordination
 606 into the M1 site (*cf.* Olin and Wolff, 2010; Reguir et al., 2012). Lattice-strain
 607 parameters as obtained from fits to the data are shown in Table S1.

608 In some low-aegirine experiments and the Canary Islands rocks, lattice-
 609 strain fitting for 3+ ions at the M1 site was not possible, because too few
 610 HREE partitioned onto the M1 site of these clinopyroxene. Here, we chose

611 to fit only lattice-strain parameters for the M2 site, or fix D_0^{3+} values for the
612 M1 site to match those for the M2 site, and fit only the r_0 and E_s parameters
613 for the M1 site. Fitting of element-partitioning data for 1+, 2+ and 4+ ions
614 was less successful owing to sparse coverage of suitable radii and detection-
615 limit issues for some elements. Partition coefficients for 1+, 2+, and 4+
616 elements follow radius- and charge-dependent trends consistent with lattice-
617 strain theory and reported effects of charge on lattice-strain parameters (Fig.
618 8b, e.g., Hazen and Finger, 1979; Law et al., 2000; Adam and Green, 2006).

619 *5.4.1. Effects of composition on ideal site size, r_0*

620 As the composition of clinopyroxene shifts from augite toward aegirine,
621 the size of the M1 and M2 sites, or strain-free radii (r_0), should diverge fol-
622 lowing the sizes of the major-element cations on these sites. Lattice-strain fits
623 for 3+ cations indicate expansion of the M2 site between low and medium-
624 aegirine clinopyroxene, with r_{0M2}^{3+} correlating well with Na replacing Ca (Figs.
625 8, 9). Expansion of the M2 site stalls at $r_{0M2}^{3+} \approx 1.12$ Å and $X_{Na}^{M2} \approx 0.4$,
626 changing little in size between medium and high-aegirine clinopyroxene. We
627 suggest that this is a ‘saturation effect’, whereby the smaller ions in the T
628 and M1 sites prevent further expansion of the M2 site as additional R_{M2}^{3+}
629 is added to the clinopyroxene. For the M1 site of clinopyroxene, strain free
630 radii for R^{3+} cations indicate expansion between low and medium-aegirine
631 clinopyroxene and contraction between medium and high-aegirine clinopy-
632 roxene (Figs. 8, 9). These trends broadly follow the substitution of Mg^{2+} for
633 Fe^{2+} , then Fe^{2+} for Fe^{3+} with increasing aegirine content in the clinopyrox-
634 ene.

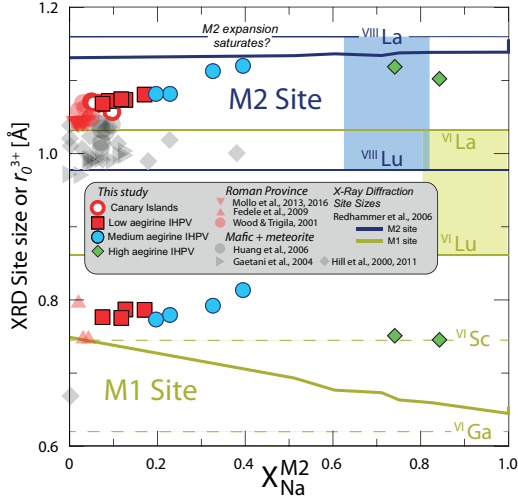


Figure 9: Diagram showing variation of ideal ionic radius r_0^{3+} with X_{NaM2} for M1 and M2 sites of clinopyroxene. Shown for comparison are single crystal x-ray diffraction data from the hedenbergite-aegirine compositional join (heavy solid lines, from Redhammer et al., 2006). Shaded boxes represent the range of ionic radii for rare earth elements in VI and VIII coordination (Shannon, 1976). Literature data for the Roman Province, Italy are from Fedele et al. (2009); Mollo et al. (2013, 2016); Wood and Trigila (2001) and for mafic systems are from Hill et al. (2000, 2011); Gaetani (2004); Huang et al. (2006).

635 5.4.2. The effect of cation charge on the D_0 parameter

636 The D_0 parameter of the lattice-strain model describes ideal, strain-free
 637 partitioning and tracks the solubility of an ideal cation in the mineral with
 638 changing pressure, temperature and the bulk composition of the system
 639 (Wood and Blundy, 2014). D_0 therefore correlates with the major-element
 640 composition of the clinopyroxene. Moreover, incorporation of trace-elements
 641 of a different charge introduces an electrostatic penalty that leads to a lower
 642 D_0 for that charge (Wood and Blundy, 2001, 2003).

643 The average charge of major-elements on the M2 site of clinopyroxene

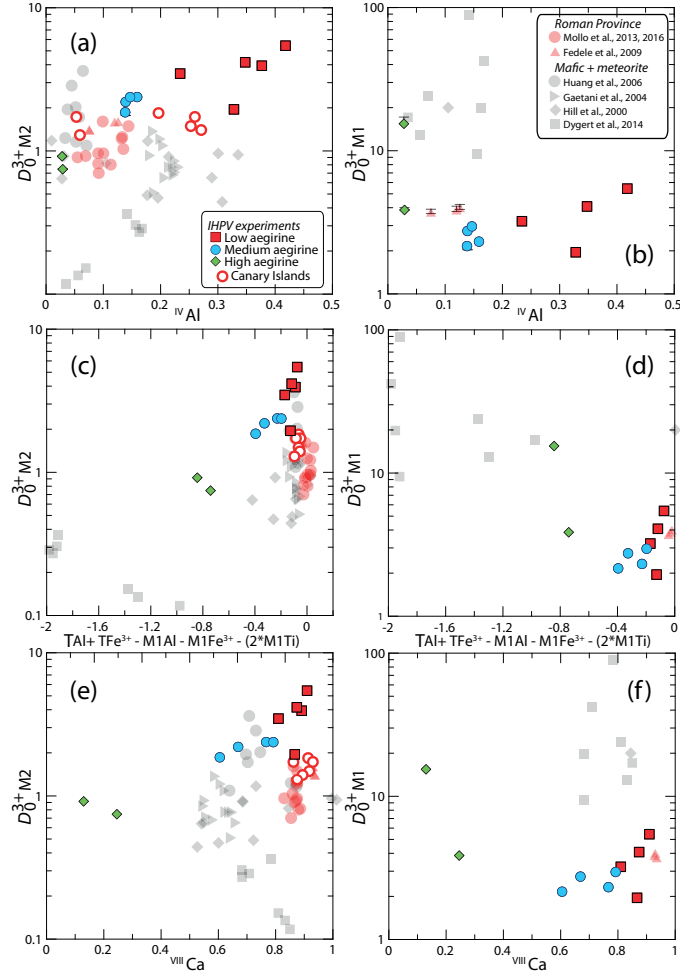


Figure 10: Strain-free partitioning coefficients (D_0) for 3+ ions into clinopyroxene vs. various charge compensation mechanisms. (a,c,e) are for the M2 site, and (b,d,f) are for the M1 site. The diagrams show that variability in partitioning behaviour is highly dependent on mineral composition, and that variation between aegirine-rich clinopyroxene cannot be explained well by the same mechanisms as more mafic systems. Literature data for element-partitioning in Mafic + Meteorite and Roman Province compositions are from the compilation of Bédard (2014). 1σ uncertainties are shown in (a, b) and are usually smaller than the symbol sizes.

decreases from 2+ to 1+ on the compositional join between Ca-rich diopside and Na-rich aegirine. Consequently, the electrostatic penalty for substituting a REE³⁺ cation into the clinopyroxene M2 site is increased. Indeed, $D_{0,M2}^{3+}$ decreases as Ca exchanges for Na (Fig. 10e). Conversely, as the average charge on the M1 site of clinopyroxene increases from 2+ toward 3+ in end-member aegirine, the electrostatic penalty incurred when substituting REE³⁺ cations onto the M1 site is reduced (Fig. 10f). As a result, $D_{0,M1}^{3+}$ increases by approximately an order of magnitude between our medium-aegirine and high-aegirine experimental clinopyroxene, an effect that when combined with the shrinking M1 site size, leads to strong fractionation of the HREE (Figs. 8 and 10f).

A positive correlation between Al^T and partition coefficients for highly charged trace-elements has been extensively documented in studies on clinopyroxene (Lundstrom et al., 1994; Gaetani and Grove, 1995; Blundy et al., 1998; Francis and Minarik, 2008; Hill et al., 2011; Mollo et al., 2016). The low-aegirine experimental clinopyroxene and most of the Canary Islands rocks extend trends defined by clinopyroxene from mafic systems (Fig. 10a), whereas the remainder of the experimental data set and Canary Islands rocks show element-partitioning behaviour similar to the potassic Roman Province of Italy (Wood and Trigila, 2001; Fedele et al., 2009; Mollo et al., 2016), confirming that an Al^T-controlled substitution mechanism extends to peralkaline conditions (Figs. 7, 10a).

Tetrahedral Al is thought to facilitate incorporation of REE³⁺ cations onto the M2 site of clinopyroxene by replacing Si⁴⁺, thereby reducing local charge and thus the electrostatic penalty associated with incorporation of

669 REE (Blundy et al., 1998). The substitution of Fe³⁺ for tetrahedral Si⁴⁺ can
670 be expected to have a similar effect. Conversely, R³⁺ ions on the neighbouring
671 M1 site should hinder incorporation of REE on the M2 site, because they
672 increase local charge by replacing R²⁺ ions, such as Mg²⁺ and Fe²⁺. This
673 electrostatic penalty should apply doubly to Ti⁴⁺ on the M1 site. This effect
674 is consistent with our experimental data (Fig. 10c), but is not obvious in the
675 natural samples, nor in the majority of the literature experimental data. It
676 would thus appear that other factors, such as melt structure, have a stronger
677 control on D_{REE} (e.g. Prowatke and Klemme, 2005).

678 D_0^{3+} parameters for the M1 site are strongly correlated with those for the
679 M2 site, except at aegirine concentrations exceeding 50 mol.%. Similarities to
680 M2 partitioning behaviour likely reflect the dominance of T-site substitution
681 mechanisms in augite clinopyroxene. In the high-aegirine clinopyroxene, T-
682 site substitutions become less important as the T-sites become saturated with
683 Si⁴⁺ (Fig. 5). The replacement of Fe³⁺ at the M1 site by 3+ trace-elements
684 does introduce a charge penalty, therefore D_{0M1}^{3+} increases accordingly.

685 *5.5. The effects of melt structure on element-partitioning*

686 The partitioning of trace-elements between crystals and melts is con-
687 trolled by their relative activity in each phase and the exchange mechanisms
688 by which their incorporation into crystals takes place (e.g., Jd-melt, Jd-DiHd
689 and CaTS-DiHd exchanges have been shown to control REE incorporation
690 in cpx, Putirka, 2008; Wood and Blundy, 2014; Mollo et al., 2017). As such,
691 one might expect to see correlations between melt structural parameters and
692 trace-element-partition coefficients. Such correlations have been reported by
693 numerous authors (e.g., Schmidt et al., 2006; Mollo et al., 2017), but appear

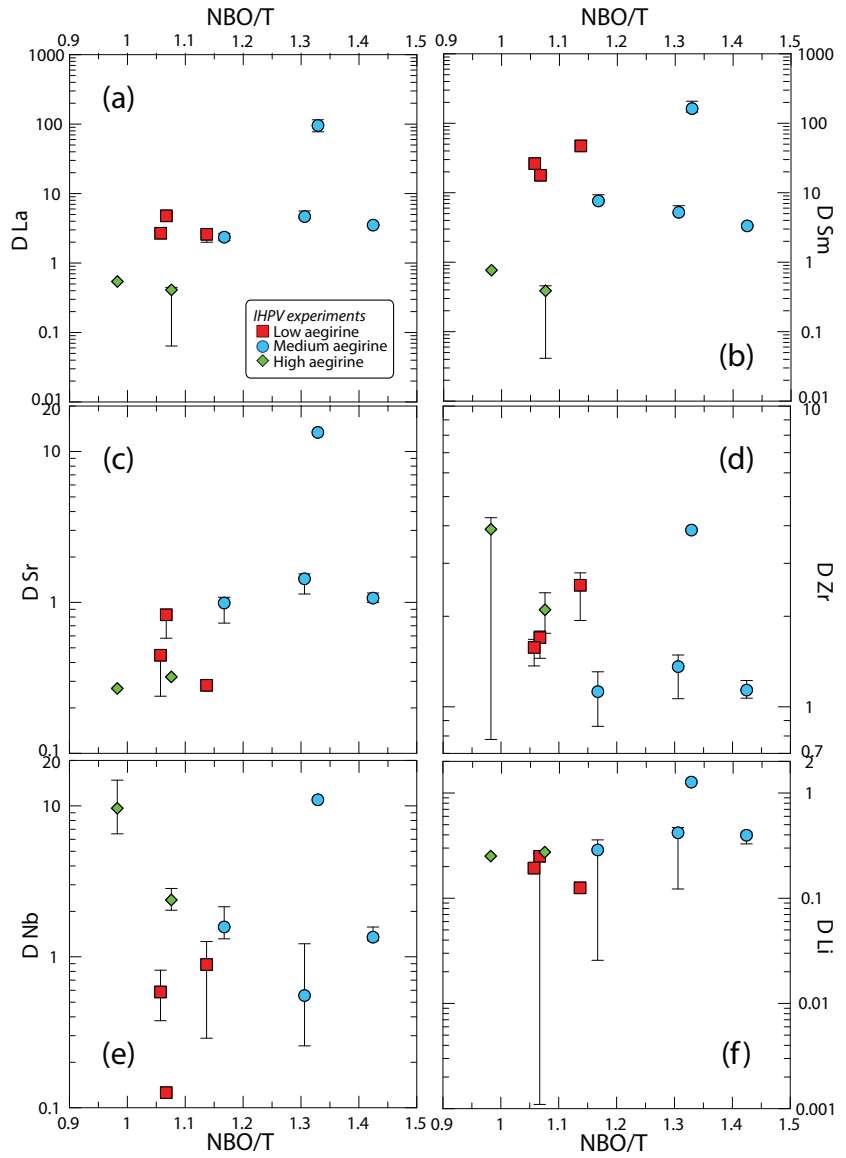


Figure 11: Diagrams of clinopyroxene–melt trace-element-partition coefficients for the IHPV experiments as a function of NBO/T of the quenched melt (Mysen et al., 1985). The water-saturated, sodic compositions investigated produce melts with highly depolymerised structures. The NBO/T ratio of these melts is not correlated with trace-element-partition coefficients, except weakly in the case of Sr. In highly polymerised systems ($\text{NBO}/\text{T} < 0.49$, Gaetani 2004) partition coefficients for REE and HFSE are negatively correlated with this parameter. (see Fig. 9 from Huang et al. 2006).

694 to be expressed over a limited range of melt compositions (Gaetani, 2004;
695 Huang et al., 2006). A widely used descriptor for melt structure is the ra-
696 tio of non-bonding oxygen anions to tetrahedrally-coordinated cations ($\frac{NBO}{T}$,
697 Mysen et al., 1982, 1985). In relatively polymerised melts, where this ratio
698 falls below 0.49, melt structure has been shown to have a significant influence
699 on mineral–melt partition coefficients (Gaetani, 2004; Huang et al., 2006).

700 To calculate NBO/T for our experiments, we estimated melt Fe oxida-
701 tion state from run temperatures and known fO_2 buffer conditions (Kress
702 and Carmichael, 1991). The recalculated total of major-element oxides (incl.
703 Fe_2O_3) was then used to approximate the water content of the quenched
704 melts. Oxygen from this dissolved water was added into the NBO/T cal-
705 culation, which followed Mysen et al. (1985). The high content of alka-
706 lies and dissolved water in the experiments presented here produced melts
707 that have $NBO/T = 0.98\text{--}1.42$; well above the compositional boundary re-
708 ported by Gaetani (2004). Consistent with his findings, most trace-element-
709 partition coefficients determined from our experiments are uncorrelated with
710 the NBO/T ratio of the melt (Fig. 11). An exception is D_{Sr} that shows
711 a weak positive correlation with NBO/T (Fig. 11c). NBO/T could not be
712 calculate for our Canary Islands compositions because the water content of
713 the melt prior to quench is not known.

714 Because partition coefficients between clinopyroxene and melt are con-
715 trolled by the relative activity of elements in each of these two phases, an
716 empirical model to predict partition coefficients from both melt and mineral
717 compositional terms has the highest potential for accuracy. Application of
718 such a model would however require measurement of both mineral and melt

719 phases, which would limit its geological utility. A similar model based only
720 on clinopyroxene composition could be applied in a wider range of scenarios
721 where melt composition cannot be directly measured, for example to cumu-
722 late systems or to concentrically zoned phenocrysts. Because crystallisation
723 is a thermodynamically controlled process, the composition of the melt and
724 thus its effects on element-partitioning will, at least in part, be recorded by
725 the composition of the clinopyroxene. This considered, we chose to calibrate
726 a clinopyroxene-based empirical partitioning model, based on lattice-strain
727 theory that would be applicable over a wide compositional range from tholei-
728 itic basalts to peralkaline phonolites. Details are provided in the following
729 sections.

730 *5.6. An element-partitioning model extending to aegirine clinopyroxene*

731 Element partition coefficients vary systematically with the physiochemi-
732 cal conditions of natural and synthetic magmas (cf. Wood and Blundy, 2003).
733 Consequently, a host of models have been presented to describe the system-
734 atics of element-partitioning between clinopyroxene and silicate melts (Wood
735 and Blundy, 1997, 2001; Hill et al., 2011; Yao et al., 2012; Sun and Liang,
736 2012; Bédard, 2014; Dygert et al., 2014; Mollo et al., 2016). The majority of
737 these models are based on lattice-strain theory and predict how the lattice
738 parameters r_0 , E_s , and D_0 vary with composition, temperature and pressure.
739 This semi-thermodynamic approach theoretically permits calculation of par-
740 tition coefficients for any trace-element, at any set of $P - T - X$ conditions.
741 In reality, all models have a limited working range, as restricted by the input
742 data set. Because existing partitioning models do not reproduce the high
743 $r_{0,M2}^{3+}$ values for clinopyroxene with aegirine contents ≥ 50 mol % (Fig. 12a),

744 they cannot accurately predict REE partitioning behaviour for strongly per-
745 alkaline systems. Here, we present a new empirical model that is calibrated
746 on both our experimental work and natural partition coefficients from Ca-
747 nary Islands rocks, as well as existing partitioning data from the literature
748 (compilation of Bédard, 2014, Fig. 12, Table S1).

749 Our model focuses on the dependence of element-partitioning on clinopy-
750 roxene composition, temperature and pressure only. While partition coeffi-
751 cients are thermodynamically controlled by activity of elements in both the
752 crystal and the melt phase (Wood and Blundy, 2014), and while melt struc-
753 ture has been shown to influence element-partitioning (Huang et al., 2006;
754 Schmidt et al., 2006; Mollo et al., 2017), it is not always possible to measure
755 melt composition directly. For example, equilibrium melt compositions can-
756 not be measured for the cores of zoned clinopyroxene phenocrysts in tephra,
757 or indeed for any crystal from an intrusion in which gravitational segrega-
758 tion of phases has occurred. Therefore, while the predictive power of a model
759 based only on the compositions of the crystal should be lower than that of
760 a model based on both crystal and melt compositions, a crystal-only model
761 may be applied to a wider spectrum of geological scenarios. Melt composi-
762 tion should, at least in part, be recorded by the major-element composition
763 of the clinopyroxene.

764 *5.6.1. The clinopyroxene M2 site*

765 To find the principal physiochemical factors that affect element-partitioning
766 at the M2 site of clinopyroxene, a stepwise least-squares multiple linear re-
767 gression analysis was performed using the lattice-strain parameters r_0^{3+} , E_s^{3+}
768 and D_0^{3+} , temperature, pressure and clinopyroxene composition as inputs.

769 Input parameters were initially examined in binary scatter diagrams to as-
770 certain whether correlations with lattice-strain parameters were linear. If
771 not, interaction compositional terms were added to the initial set of possible
772 fitting parameters that had linear correlations with lattice-strain parameters
773 (e.g. $X_{Al+Fe^{3+}}^T$). Intensive variables for multiple regression models for r_0 ,
774 E_s and D_0 were introduced following a hierarchical forward selection crite-
775 rion with switching. The largest number of significant terms to describe a
776 lattice-strain parameter was eight for E^{M2} (c.95%, cf. Supplement S4).

777 Because of systematic covariation of compositional parameters in our
778 small data set of experiments and natural samples ($n = 16$), a model cal-
779 ibrated with these points alone would be unable to deconvolve the effects
780 of each major-element on partitioning behaviour. We have therefore added
781 published experiments and natural phenocryst-glass pairs ($n = 75$) to assem-
782 ble a database covering a wide range of composition, pressure, temperature
783 and oxygen fugacity (data from compilation of Bédard 2014, and Mollo et al.
784 2016, 0.0001–3.5 GPa, 650–1345 °C, $\log fO_2 = IW$ to $MH \approx \Delta QFM -5$
785 to +5). clinopyroxene compositions cover XMg 0.031–1, X_{Na}^{M2} 0–0.84 and
786 Al^T 0–0.49 c.f.u. and melt compositions vary widely in terms of Mg# (0–
787 100) and XH_2O (0–0.38). REE partition coefficients also vary significantly
788 (e.g. D_{La} 0.01–4.79; D_{Sm} 0.02–47.24, and D_{Yb} 0.11–8.00). The majority
789 of partition coefficients in the training data set were measured via SIMS
790 or LA-ICP-MS, minimising analytical uncertainty (e.g. from analyses by
791 electron-microprobe).

792 The resultant empirical model accounts well for changes in lattice-strain
793 parameters over a range of compositions from basalt to peralkaline phono-

794 lite, faithfully reproducing large r_0^{M2} values typical for sodic clinopyroxene
 795 (Fig. 12, model coefficients in Table 5). Student t-tests show that all of the
 796 independent variables included in the models are significant at the 95% con-
 797 fidence level and PRESS R^2 values were obtained by repeatedby randomly
 798 subsampling the dataset (Stevens, 1996), are close to R^2 values calculated by
 799 regular methods, indicating robust models with high predictive power. Full
 800 multiple regression reports are available in Supplement S4. Equations gen-
 801 erated by the multiple linear regression calculations are given below for the
 802 M2 site, where a_i are the regression coefficients for the respective variables:
 803

$$\ln D_0^{M2} = a_1 + a_2 T + a_3 X_{Al+Fe^{3+}}^T + a_4 X_{Ti}^{M1} + a_5 X_{Al-Fe^{3+}}^{M1} + a_6 X_{Fe^{2+}}^{M2} \quad (3)$$

$$E^{M2} = a_7 + a_8 P + a_9 X_{Al+Fe^{3+}}^T + a_{10} X_{Al}^{M1} + a_{11} X_{Mg}^{M1} + a_{12} X_{Ti}^{M1} \\ + a_{13} X_{Mg}^{M2} + a_{14} X_{Mg} \quad (4)$$

$$r_0^{M2} = a_{15} + a_{16} T + a_{17} X_{Al-Fe^{3+}}^{M1} + a_{18} X_{Ti}^{M1} + a_{19} X_{Ca}^{M2} + a_{20} X_{Na}^{M2} \quad (5)$$

804 The model for r_0^{M2} is robust with high predictive power and incorporates
 805 compositional controls from the M1 and M2 sites, as well as temperature.
 806 Elevated concentrations of large M2 cations Ca^{2+} and Na^+ are correlated
 807 with large M2 sites. Ti^{4+} cations in the neighbouring M1 site are also cor-
 808 related with expansion of the M2 site, and the concentration of small Al^{3+}
 809 minus larger Fe^{3+} on the M1 site is negatively correlated with r_0^{M2} . The neg-
 810 ative correlation between r_0^{M2} and temperature reflects the sum of changes

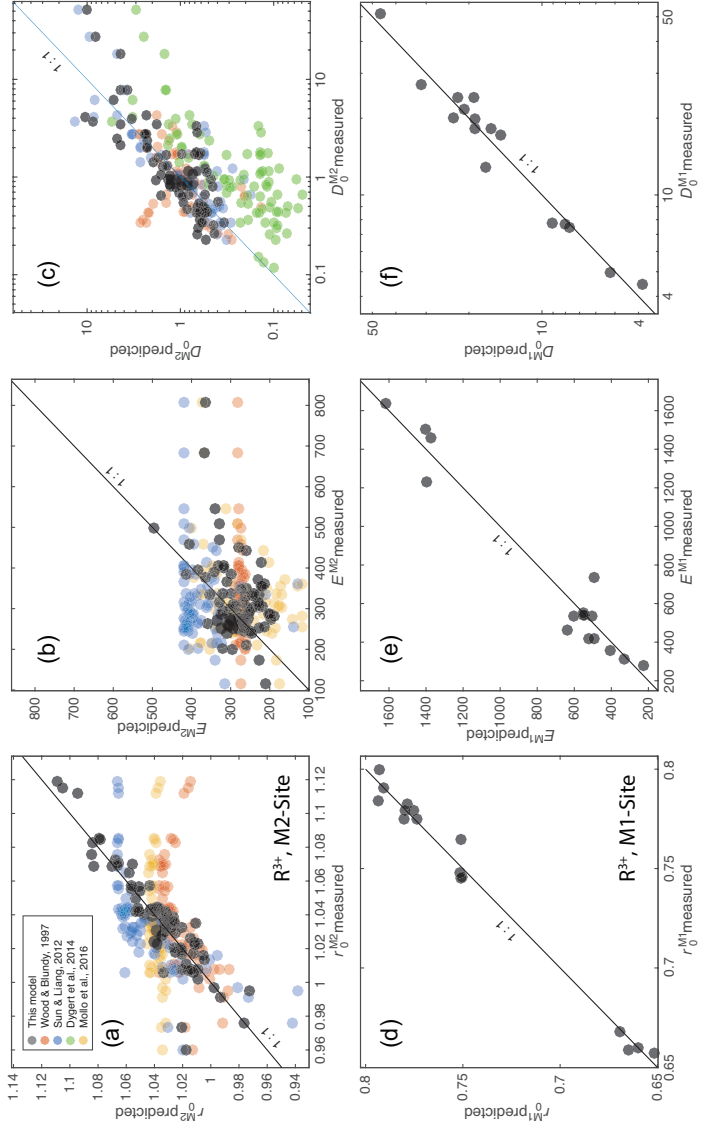


Figure 12: Measured vs. predicted model values for lattice-strain parameters for the M2 and M1 sites of clinopyroxene. The new models presented here were generated via a stepwise multiple linear regression procedure following a hierarchical forward selection criterion with switching. Full regression reports are in Supplement S4 and model equations are in the main text.

811 to major-element composition that lead to smaller clinopyroxene M2 sites at
812 higher temperatures. This compositional effect swamps the minor influence
813 of thermal expansion.

814 D_0^{M2} is reasonably well predicted and incorporates compositional terms
815 from all three sites in clinopyroxene and temperature. The positive effect
816 of tetrahedral R³⁺ on D_0^{M2} is the largest contribution to the model, which
817 is consistent with published studies (see above). The relationship between
818 clinopyroxene compositional terms on the M1 and M2 sites and D_0 are in-
819 direct and are tied to the solubility of the mineral in the melt (Wood and
820 Blundy, 2003), which in turn is tied to the physiochemical conditions of the
821 system (largely melt composition). The model for D_0^{M2} is less robust than
822 that for r_0^{M2} , largely because there are melt compositional effects that are
823 not recorded in the composition of the clinopyroxene. We tested the Mg#
824 and XH₂O of the melt, neither of which are significant predictors for D_0^{M2} .

825 The model for E^{M2} is less well-constrained than for the other two M2
826 lattice-strain parameters, suggesting that M2 site stiffness is not tied strongly
827 to clinopyroxene composition, temperature or pressure. Despite a signifi-
828 cantly lower predictive power, this model still has physical grounding. Stiff-
829 ness of the M2 site is positively correlated with pressure, as might be expected
830 following a simple Hooke's law relationship, and there are some subtle com-
831 positional controls imparted by the T and M1 sites. The poor correlation
832 between E^{M2} , clinopyroxene composition, temperature and pressure is also
833 evident in published element-partitioning models, where E^{M2} is either poorly
834 predicted (Fig. 12b), or set to a fixed value (e.g. Dygert et al., 2014).

835 Diagrams of measured vs. predicted D values for R³⁺ cations are given in

836 Figure 13a, showing the predictive power of the models over a compositional
 837 range between basalt and peralkaline phonolite. For the M2 site, 95% of
 838 the measured R^{3+} partition coefficients are reproduced within a factor of
 839 ± 2.5 (hard dashed lines), and in extreme cases, the model still reproduces D
 840 values within an order of magnitude, sufficient for the prediction of element-
 841 partitioning trends over a wide range of $P - T - X$. D_{MREE} , such as Sm,
 842 are reproduced more faithfully than D_{LREE} , because their radius is closer to
 843 $r_0^{M^2}$ (Fig. 13c,d), and therefore prediction of their partitioning behaviour is
 844 affected less strongly by inaccuracies in predicted E^{M^2} values.

845 *5.6.2. The clinopyroxene M1 site*

846 Using a methodology similar to the M2 site, we fitted a predictive model
 847 for partitioning of R^{3+} cations onto the smaller, 6-coordinated M1 site of
 848 clinopyroxene. Lattice-strain parabola were constrained by partitioning data
 849 for Cr, Ga, Sc, and where suitable, the HREE Tm, Yb and Lu (Our IHPV
 850 experiments plus Hill et al. 2000; Fedele et al. 2009; Mollo et al. 2013; Dygert
 851 et al. 2014). The training data set for the M1 site partitioning model is
 852 small relative to that for the M2 site ($n = 18$), and because it is strongly
 853 skewed toward alkaline compositions, it has lower predictive power and is
 854 not recommended for application to mafic magmatic systems. Equations for
 855 the M1 site lattice-strain parameters, as generated by multiple linear least
 856 squares regression, are given below and shown in Figure 12 where b_i are the
 857 regression coefficients (Table 5) for the respective variables:

$$\ln D_0^{M1} = b_1 + b_2 X_{Al}^T + b_3 X_{Fe^{2+}}^{M1} + b_4 X_{Ca}^{M2} + b_5 X_{Na}^{M2} \quad (6)$$

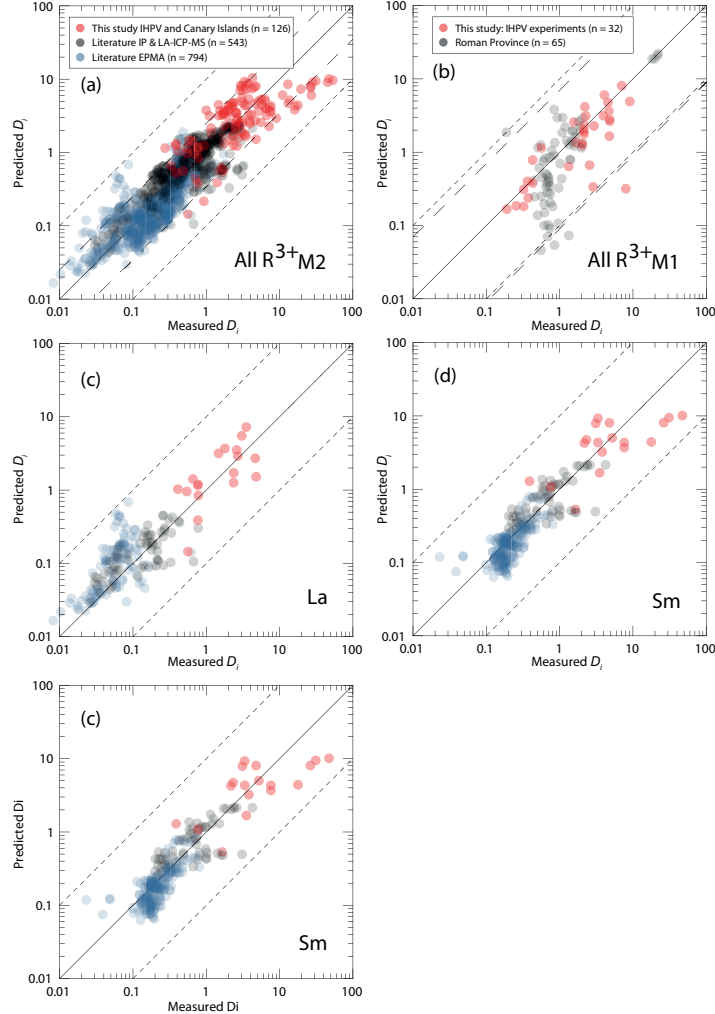


Figure 13: Measured clinopyroxene–silicate melt partition coefficients for 3+ cations vs. those predicted by our empirical model. (a) shows a comparison between measured partition coefficients and model-derived values for the M2 site of clinopyroxene. Hard dashed lines represent 95% confidence intervals of the model, and correspond to maximum uncertainties of factor $\frac{+2.5}{-2.9}$. Fine dashed lines represent 1 order of magnitude uncertainty (extreme outliers for M2 model). Partition coefficients in this diagram are the REE La to Er for our IHPV experiments, Canary Islands rocks, and literature data from the Roman Province (Wood and Trigila, 2001; Fedele et al., 2009; Mollo et al., 2013, 2016), and all the REE plus Y for the rest of the data compilation (Bédard, 2014), which is split by analytical methodology. (b) shows performance of the predictive model for the M1 site that is calibrated for alkaline magmatic systems, and includes data from our IHPV experiments and the Roman Province (Fedele et al., 2009; Mollo et al., 2013, 2016). Maximum uncertainties at the 95% confidence interval are a factor of $\frac{+7}{-11}$, higher than for the M2 site because of the smaller calibrating data set. (c) performance of the M2 site model for La, and (d) for Sm.

$$E^{M1} = b_6 + b_7T + b_8P + b_9X_{Mg}^{M1} \quad (7)$$

$$r_0^{M1} = b_{10} + b_{11}P + b_{12}X_{Mg}^{M2} + b_{13}X_{Fe^{3+}}^{M1} + b_{14}X_{Ca}^{M2} \quad (8)$$

858 The model for r_0^{M1} is robust and accurately reproduces the input data
 859 set. A negative pressure term may reflect compressional strain on the crystal
 860 lattice. Large Fe^{3+} cations have a positive effect on the size of the M1 site,
 861 while smaller Mg^{2+} cations on the neighbouring M2 site have a negative effect
 862 on M1 site size. The small negative X_{Ca}^{M2} term is indirectly related to the
 863 size of the M1 site.

864 E^{M1} is predicted more accurately than E^{M2} and is largely described by
 865 variations in temperature and pressure. Much like the M2 site, stiffness of
 866 the M1 site appears to be controlled dominantly by physicochemical factors
 867 that are not recorded in the composition of the clinopyroxene.

868 The model for D_0^{M1} contains compositional terms from all three crystal-
 869 lographic sites in clinopyroxene. X_{Al}^T has a strong positive correlation with
 870 D_0^{M1} , consistent with a charge compensation mechanism that aids incorpora-
 871 tion of R^{3+} cations, while terms for M1 and M2 site cations may be indirectly
 872 recording melt compositional effects. Because D_0^{M1} is unusually high for our
 873 high-aegirine experiments, they had to be excluded from the fitting procedure
 874 to permit model convergence. The models for r_0^{M1} and E^{M1} are calibrated
 875 for use all the way to end-member aegirine, but this was not possible for the
 876 D_0^{M1} term, which is calibrated for use up to $\sim Ae_{50}$. Further experiments
 877 at conditions between those that generated our medium and high-aegirine

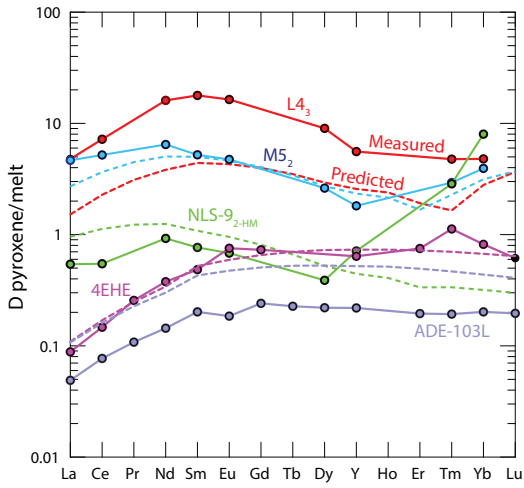


Figure 14: Measured and predicted element-partition coefficients for REE^{3+} . The model does not introduce notable radius-dependent biases, except for in our high-aegirine clinopyroxene (NLS-9₂-HM in green) for which D_{HREE} are strongly underpredicted, owing to inaccurate return of D_0^{M1} . Shown for comparison are two diopside–melt pairs: 4EHE from Hill et al. (2000), grown from a synthetic (NCMAS) basaltic andesite composition and ADE-103L from Lofgren et al. (2006) grown from a picritic composition based on the Angra dos Reis meteorite.

878 clinopyroxene would be required to better constrain the clinopyroxene com-
879 positional record of D_0^{M1} in strongly peralkaline Fe-rich magmas.

880 When applied to our experimental data, and the compilation of partition
881 coefficients from the Roman Province (Fedele et al., 2009; Mollo et al., 2013,
882 2016), the M1 stepwise model reproduces element-partitioning data to a fac-
883 tor of $\frac{+7}{-11}$ at the 95% confidence interval (Fig. 13b). Full regression reports
884 are provided in Supplement S4.

885 For convenience, we provide an EXCEL spreadsheet for calculation of
886 clinopyroxene-melt element-partition coefficients for any trace-element of 3+
887 valence that is large enough to fit onto the M1 or M2 sites of clinopyroxene
888 (Supplement S5). To assess the utility of the partitioning models and to
889 monitor for potential introduction of radius-dependent bias, we show pre-
890 dicted REE patterns normalised to measured ratios for some literature data
891 and our internally heated pressure vessel experiments (Fig. 14). The model
892 accurately reproduces REE patterns at all compositions, except for HREE
893 on the M1 site of clinopyroxene at aegirine contents exceeding ~50 mol%
894 (NLS experiments).

895 *5.7. Implications for formation of REE deposits in evolved alkaline intrusions*

896 The solubility of REE and HFSE minerals is strongly enhanced in peral-
897 kaline melts (Watson, 1979; Linnen and Keppler, 1997; Boehnke et al., 2013;
898 Aseri et al., 2015), thus the high concentration of these elements in peralka-
899 line systems may (partially) reflect this fact (Dostal, 2017). Melts containing
900 high concentrations of REE and HFSE are thought to be generated through
901 low degrees of partial melting in the source, followed by residual enrichment
902 during protracted fractional crystallisation (Marks and Markl, 2017). The

903 budget of REE and HFSE in a fractionating magma is influenced by the
904 mineralogy of the crystallising assemblage, and the extent to which these
905 elements are incorporated at minor or trace concentrations.

906 Pyroxene is a major ferromagnesian phase that is commonly saturated
907 throughout the entire differentiation histories of peralkaline magmatic sys-
908 tems (Ablay et al., 1998; Marks and Markl, 2001; Möller and Williams-Jones,
909 2016). The composition of the fractionating clinopyroxene has a major im-
910 pact on the absolute REE concentrations and REE pattern of the resid-
911 ual melt, and ultimately on the ability of a system to develop economic
912 concentrations of the REE (Fig. 15, e.g. Kogarko, 1990; Sørensen, 1992;
913 Marks et al., 2011). Pyroxene in alkaline magmatic systems is initially cal-
914 cic for mafic melts, and becomes increasingly sodic as crystal fractionation
915 proceeds (Marks et al., 2004). Although the REE are compatible in the
916 majority of our experimentally generated clinopyroxene, those approaching
917 aegirine end-member composition, as found in evolved alkaline magmatic
918 systems have the lowest D_{REE} values (Fig. 6). Strongly alkaline magmatic
919 systems are thought to crystallise abundant Ca-pyroxene early in their evolu-
920 tion which may deplete residual liquids with respect to REEs. Consequently,
921 even though crystallisation of Na-pyroxene could enrich residual liquids with
922 REE, the resultant concentration of these metals in the melt would remain
923 low. However, clinopyroxene is not the only phase to crystallise from alka-
924 line magmas, and the majority of additional silicate phases, such as olivine,
925 biotite and feldspar have $D_{REE} << 1$, typically 1-4 orders of magnitude
926 lower than clinopyroxene (Larsen, 1979; Kovalenko et al., 1988; Mahood and
927 Stimac, 1990). Consequently, if the mode of clinopyroxene is low enough,

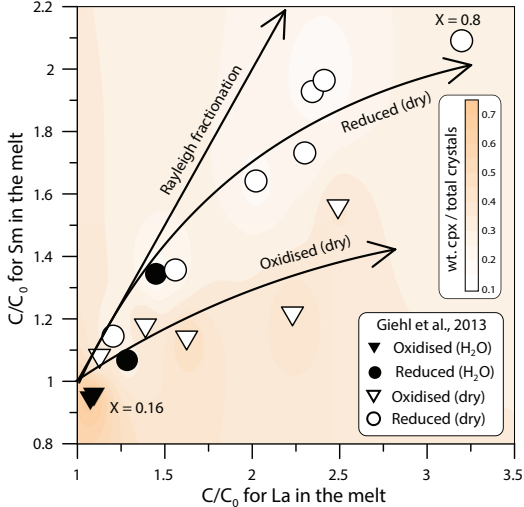


Figure 15: Model enrichment paths for La and Sm in residual melts during fractional crystallisation of a MiKa dyke composition (Gardar Province, Greenland, see Marks and Markl 2003). Phase relations and clinopyroxene compositions are from Giehl et al. (2013) and pertain to both oxidising and reducing conditions ($\log f\text{O}_2 = \Delta\text{QFM} -3$ and +1), nominally dry to water bearing (to 3 wt.% H_2O at 1 kbar). Colour shading indicates the weight fraction of clinopyroxene within the crystallising assemblage. Bold arrows indicate residual enrichment pathways for the REE in the melt for Rayleigh fractionation (no incorporation into crystals), reduced, dry conditions, and oxidised dry conditions (the latter two are hand drawn fits to the data). For simplicity, this model does not consider REE incorporation into magnetite, alkali-feldspar, olivine, nepheline or aenigmatite, all phases generated in the experiments of Giehl et al. (2013) (see Larsen, 1979; Kovalenko et al., 1988; Mahood and Stimac, 1990).

928 the bulk D_{REE} of the crystallising assemblage would remain below unity,
 929 allowing the REE to become enriched in the residual silicate melt.

930 To give insight into the optimum conditions for residual magmatic en-
 931 richment of the REE in alkaline systems we modelled the evolution of REE

932 concentrations in the melt during fractional crystallisation of a nepheline
933 syenite body (Fig. 15). Phase relation data and clinopyroxene compositions
934 are from the experimental study of Giehl et al. (2013). Their starting com-
935 position, based on the MiKa dyke, from the Gardar Province, Greenland, is
936 already extremely evolved, with $Mg\# = 2$, $(Na + K)/Al = 1.44$ and $FeO^* = 12$ wt.%.

938 In these models, crystallisation under water-bearing, oxidising conditions
939 produces a high fraction of clinopyroxene that depletes residual melts with
940 respect to Sm, while subtly enriching La. Dry conditions promote abun-
941 dant alkali feldspar (Afs) crystallisation, which effectively enriches the REE
942 content of residual melts. Under oxidising, dry conditions, the La/Sm ra-
943 tio of the residual melt increases with fractionation, because Sm is more
944 effectively incorporated into clinopyroxene. Residual enrichment is most ef-
945 fective under dry, reducing conditions because of a relatively lower fraction
946 of clinopyroxene within the crystallising assemblage. Because of this, the
947 REE enrichment path of the residual melt is close to that of ideal Rayleigh
948 fractionation. Under these reducing, dry conditions and at a temperature of
949 750°C, the experiments of Giehl et al. (2013) attained a crystal fraction of
950 0.8. Here, residual melts would have and 3.2 times La concentration and 2
951 times the Sm concentration relative to their starting composition.

952 Considering these mechanisms, alongside our experimental and Canary
953 Islands data, the best systems to develop high REE concentrations are those
954 that would produce small proportions of Ca-pyroxene early in their crystalli-
955 sation histories, quickly evolving to more sodic compositions that crystallise
956 aegirine clinopyroxene. Cooling under low-pressure, dry, reducing conditions

957 produces abundant alkali feldspar that in the case of a peralkaline compo-
958 sition, would serve to further increase the alkalinity of the residual melt.
959 Low degrees of source melting would produce primary melts with (1) high
960 REE concentrations and (2) low melt Mg + Fe, and low modal abundance
961 of clinopyroxene, which would aid enrichment in residual melts via fractional
962 crystallisation.

963 The HREE-rich nature of peralkaline magmatic systems, both granites
964 and nepheline syenites, is compatible with fractionation of moderately sodic
965 clinopyroxene that have high D_{LREE}/D_{HREE} (e.g. Möller and Williams-
966 Jones, 2016; Dostal, 2017). As crystal fractionation progresses and clinopy-
967 roxene compositions evolve toward the aegirine end-member composition,
968 D_{LREE}/D_{HREE} decreases (Fig. 6). This systematic change in element-
969 partitioning behaviour would result in strong HREE enrichment in aegirine-
970 pyroxene cumulates, and would enrich the residual melt with respect to
971 LREE-MREE.

972 Conclusions

- 973 • Our experiments reveal three distinct element-partitioning behaviours
974 for Na-rich clinopyroxene that depend on aegirine content. Each of
975 these is associated with a distinct major-element exchange vector. We
976 do not have the compositional resolution to know if the transition be-
977 tween these behaviours is smooth or step-like.
- 978 • Fits to the lattice-strain model of Blundy and Wood (1994) indicate
979 expansion of the M2 site with increasing $\text{Na}_{\text{M2}}^{+}$, to a maximum $r_{0,\text{M2}}^{3+}$ of

980 1.12 Å at $\text{Na}_{\text{M}2}^+ = 0.4$ c.f.u. Further expansion did not occur at higher
981 Na contents.

982 • Both the M1 and M2 sites shrink at high-aegirine contents in response
983 to increasing $\sum \text{R}_{\text{M}1}^{3+}$.

984 • Charge effects lead to a progressive increase in D_0^{M1} at the expense
985 of D_0^{M2} , as the exchanges Ca^{2+} for Na^+ and M^{2+} for Fe^{3+} take place.
986 Much like in systems of lower alkalinity, REE incorporation into clinopy-
987 roxene is dominated by coupled Al–Si substitutions at the T-site.

988 • Existing predictive models for clinopyroxene/melt element-partitioning
989 do not accurately reproduce the large M2 site ($r_{0,M2}^{3+}$) of clinopyroxene
990 with aegirine content exceeding 50 mol%. We have calibrated a new
991 empirical model that may be applied to any composition between basalt
992 and peralkaline phonolite, based on our data from experiments and
993 natural systems, as well as a large compilation of partition coefficients
994 from the literature.

995 • Crystallisation of abundant Ca-Mg rich clinopyroxene depletes the resid-
996 ual melts of REE, and inhibits or terminates magmatic enrichment
997 processes.

998 • Element partitioning systematics suggest that nepheline syenites which
999 host REE deposits must originate from low-degree melts with sufficient
1000 alkali enrichment to saturate clinopyroxene similar to our medium-
1001 aegirine clinopyroxene (Ae_{25--50}). Fractionation of such clinopyroxene
1002 enriches residual melts with respect to the HREE, in accord with the

1003 composition of REE-mineralised nepheline syenite systems.

1004 **Acknowledgements**

1005 We thank the Geo.X partners GFZ and Universität Potsdam for access to
1006 the HP-GeoMatS Lab, Don Baker for assistance with preparation of starting
1007 materials, Bruce Watson and Volker Möller for providing samples of Mud
1008 Tank zircon and the Nechalacho rocks, respectively, Hans Peter Nabein,
1009 Maria Stuff and Julia Pohlenz for assistance with HP experimental equip-
1010 ment, Toby Soutar for help with preparation of the Canary Islands samples,
1011 Lang Shi and Glenn Poirier for assistance with electron-microprobe analyses,
1012 and Anna Jung for assistance with laser ICP-MS analyses. The manuscript
1013 benefited from discussions with Longbo Yang, Rebecca Paisley, Shane Rooy-
1014 akkers and Jean Bédard. Silvio Mollo, Lorenzo Fedele and an anonymous
1015 reviewer are thanked for their insightful feedback. Nelson Eby is thanked for
1016 editorial handling. This work was funded by PhD scholarships to C.B. from
1017 Geotop, DIVEX, and the SEG Canada Foundation, and operating grants to
1018 V.vH. and J.S. from the Natural Sciences and Engineering Research Coun-
1019 cil of Canada (grant numbers RGPIN-2014-05955, RGPAS-462335-2014) and
1020 the FQRNT team research project program.

1021 **References**

- 1022 Ablay, G.J., Carroll, M.R., Palmer, M.R., Martí, J., Sparks, R.S.J.,
1023 1998. Basanite–phonolite lineages of the Teide–Pico Viejo volcanic
1024 complex, Tenerife, Canary Islands. *Journal of Petrology* 39, 905–936.
1025 doi:10.1093/petroj/39.5.905.

- 1026 Ablay, G.J., Ernst, G.G.J., Marti, J., Sparks, R.S.J., 1995. The 2 ka sub-
1027 plinian eruption of Montaña Blanca, Tenerife. *Bulletin of Volcanology* 57,
1028 337–355. doi:10.1007/BF00301292.
- 1029 Adam, J., Green, T., 2006. Trace element partitioning between mica- and
1030 amphibole-bearing garnet lherzolite and hydrous basanitic melt: 1. Exper-
1031 imental results and the investigation of controls on partitioning behaviour.
1032 *Contributions to Mineralogy and Petrology* 152, 1–17. doi:10.1007/s00410-
1033 006-0085-4.
- 1034 Akasaka, M., Onuma, K., 1980. The join $\text{CaMgSi}_2\text{O}_6$ - $\text{CaFeAlSi}_2\text{O}_6$ -
1035 $\text{CaTiAl}_2\text{O}_6$ and its bearing on the Ti-rich fassaitic pyroxenes. *Contribu-*
1036 *tions to Mineralogy and Petrology* 71, 301–312. doi:10.1007/BF00371672.
- 1037 Albert, H., Costa, F., Martí, J., 2015. Timing of magmatic processes and
1038 unrest associated with mafic historical monogenetic eruptions in Tenerife
1039 Island. *Journal of Petrology* 56, 1945–1966. doi:10.1093/petrology/egv058.
- 1040 Andújar, J., Scaillet, B., 2012. Experimental constraints on parameters con-
1041 trolling the difference in the eruptive dynamics of phonolitic magmas: the
1042 case of Tenerife (Canary Islands). *Journal of Petrology* 53, 1777–1806.
1043 doi:10.1093/petrology/egs033.
- 1044 Aseri, A.A., Linnen, R.L., Che, X.D., Thibault, Y., Holtz, F., 2015. Effects of
1045 fluorine on the solubilities of Nb, Ta, Zr and Hf minerals in highly fluxed
1046 water-saturated haplogranitic melts. *Ore Geology Reviews* 64, 736–746.
1047 doi:10.1016/j.oregeorev.2014.02.014.

- 1048 Beard, C.D., 2018. Mineral-melt trace element partitioning in alkaline mag-
1049 matic systems. Phd thesis. McGill University.
- 1050 Bédard, J.H., 2014. Parameterizations of calcic clinopyroxene - Melt trace
1051 element partition coefficients. *Geochemistry, Geophysics, Geosystems* 15,
1052 303–336. doi:10.1002/2013GC005112.
- 1053 Behrens, H., Hahn, M., 2009. Trace element diffusion and viscous flow in
1054 potassium-rich trachytic and phonolitic melts. *Chemical Geology* 259, 63–
1055 77. doi:10.1016/j.chemgeo.2008.10.014.
- 1056 Berndt, J., Liebske, C., Holtz, F., Freise, M., Nowak, M., Ziegenbein,
1057 D., Hurkuck, W., Koepke, J., 2002. A combined rapid-quench and H₂-
1058 membrane setup for internally heated pressure vessels: description and
1059 application for water solubility in basaltic melts. *American Mineralogist*
1060 87, 1717–1726. doi:10.1029/JB089iB10p08540.
- 1061 Blundy, J., Wood, B., 1994. Prediction of crystal–melt partition coefficients
1062 from elastic moduli. *Nature* 372, 452–454. doi:10.1038/372452a0.
- 1063 Blundy, J.D., Robinson, J.A.C., Wood, B.J., 1998. Heavy REE are compat-
1064 ible in clinopyroxene on the spinel lherzolite solidus. *Earth and Planetary
1065 Science Letters* 160, 493–504. doi:10.1016/S0012-821X(98)00106-X.
- 1066 Bohnke, P., Watson, E.B., Trail, D., Harrison, T.M., Schmitt, A.K.,
1067 2013. Zircon saturation re-revisited. *Chemical Geology* 351, 324–334.
1068 doi:10.1016/j.chemgeo.2013.05.028.
- 1069 Borchert, M., Wilke, M., Schmidt, C., Cauzid, J., Tucoulou, R., 2010. Par-
1070 titioning of Ba, La, Yb and Y between haplogranitic melts and aque-

- 1071 ous solutions: An experimental study. *Chemical Geology* 276, 225–240.
1072 doi:10.1016/j.chemgeo.2010.06.009.
- 1073 Boudreau, A.E., 2004. PALLADIUM, a program to model the chromatographic separation of the platinum-group elements, base metals and sulfur
1074 in a solidifying pile of igneous crystals. *Canadian Mineralogist* 42, 393–403.
1075 doi:10.2113/gscanmin.42.2.393.
- 1077 Brown, R.J., Barry, T.L., Branney, M.J., Pringle, M.S., Bryan, S.E., 2003.
1078 The Quaternary pyroclastic succession of southeast Tenerife, Canary Islands:
1079 explosive eruptions, related caldera subsidence, and sector collapse.
1080 *Geological Magazine* 140, 265–288. doi:10.1017/S0016756802007252.
- 1081 Bryan, S.E., Martí, J., Cas, R.A.F., 1998. Stratigraphy of the Bandas del
1082 Sur Formation: an extracaldera record of Quaternary phonolitic explosive
1083 eruptions from the Las Cañadas edifice, Tenerife (Canary Islands).
1084 *Geological Magazine* 135, 605–636. doi:null.
- 1085 Carracedo, J.C., Badiola, E.R., Guillou, H., Paterne, M., Scaillet, S.,
1086 Torrado, F.J.P., Paris, R., Fra-Paleo, U., Hansen, A., 2007. Eruptive
1087 and structural history of Teide Volcano and rift zones of Tenerife, Ca-
1088 nary Islands. *Geological Society of America Bulletin* 119, 1027–1051.
1089 doi:10.1130/B26087.1.
- 1090 Carroll, M.R., Blank, J.G., 1997. The solubility of H₂O in phonolitic melts.
1091 *American Mineralogist* 82, 549–556. doi:10.1093/petrology/32.5.1021.
- 1092 Chou, I.M., 1986. Permeability of precious metals to hydrogen at 2 kb total

- 1093 pressure and elevated temperatures. *American Journal of Science* 286,
1094 638–658.
- 1095 Corgne, A., Wood, B.J., 2005. Trace element partitioning and substitu-
1096 tion mechanisms in calcium perovskites. *Contributions to Mineralogy and*
1097 *Petrology* 149, 85–97. doi:10.1007/s00410-004-0638-3.
- 1098 Costa, F., Chakraborty, S., Dohmen, R., 2003. Diffusion coupling between
1099 major and trace elements and a model for the calculation of magma cham-
1100 ber residence times using plagioclase. *Geochimica et Cosmochimica Acta*
1101 67, 2189–2200. doi:10.1016/S0016-7037(00)01345-5.
- 1102 Coumans, J.P., Stix, J., Clague, D.A., Minarik, W.G., Layne, G.D., 2016.
1103 Melt-rock interaction near the Moho: Evidence from crystal cargo in lavas
1104 from near-ridge seamounts. *Geochimica et Cosmochimica Acta* 191, 139–
1105 164. doi:10.1016/j.gca.2016.07.017.
- 1106 Deer, W.A., Howie, R.A., Zussman, J., 1992. An introduction to the rock-
1107 forming minerals. Longman Group Ltd, New York.
- 1108 Dostal, J., 2017. Rare earth element deposits of alkaline igneous rocks. *Re-*
1109 *sources* 6, 1–12. doi:10.3390/resources6030034.
- 1110 Downes, H., Balaganskaya, E., Beard, A., Liferovich, R., Demaiffe, D.,
1111 2005. Petrogenetic processes in the ultramafic, alkaline and carbonatitic
1112 magmatism in the Kola Alkaline Province: A review. *Lithos* 85, 48–75.
1113 doi:10.1016/j.lithos.2005.03.020.
- 1114 Droop, G.T.R., 1987. A general equation for estimating Fe³⁺ concentrations

- 1115 in ferromagnesian silicates and oxides from microprobe analyses, using
1116 stoichiometric criteria. *Mineralogical magazine* 51, 431–435.
- 1117 Dygert, N., Liang, Y., Sun, C., Hess, P., 2014. An experimental study of
1118 trace element partitioning between augite and Fe-rich basalts. *Geochimica
et Cosmochimica Acta* 132, 170–186. doi:10.1016/j.gca.2014.01.042.
- 1119
- 1120 Edgar, C.J., Wolff, J.A., Olin, P.H., Nichols, H.J., Pittari, A., Cas, R.A.F.,
1121 Reiners, P.W., Spell, T.L., Martí, J., 2007. The late Quaternary Diego Her-
1122 nandez Formation, Tenerife: Volcanology of a complex cycle of voluminous
1123 explosive phonolitic eruptions. *Journal of Volcanology and Geothermal Re-
1124 search* 160, 59–85. doi:10.1016/j.jvolgeores.2006.06.001.
- 1125
- 1126 Eugster, H.P., Wones, D.R., 1962. Stability relations of the ferruginous bi-
otite, annite. *Journal of Petrology* 3, 82–125. doi:10.1093/petrology/3.1.82.
- 1127
- 1128 Fedele, L., Zanetti, A., Morra, V., Lustrino, M., Melluso, L., Vannucci,
1129 R., 2009. Clinopyroxene/liquid trace element partitioning in natural
1130 trachyte–trachyphonolite systems: insights from Campi Flegrei (south-
ern Italy). *Contributions to Mineralogy and Petrology* 158, 337–356.
1131 doi:10.1007/s00410-009-0386-5.
- 1132
- 1133 Foley, S.F., Prelevic, D., Rehfeldt, T., Jacob, D.E., 2013. Minor and
1134 trace elements in olivines as probes into early igneous and mantle
1135 melting processes. *Earth and Planetary Science Letters* 363, 181–191.
doi:10.1016/j.epsl.2012.11.025.
- 1136 Francis, D., Minarik, W., 2008. Aluminum-dependent trace element parti-

- 1137 titioning in clinopyroxene. Contributions to Mineralogy and Petrology 156,
1138 439–451. doi:10.1007/s00410-008-0295-z.
- 1139 Gaetani, G.A., 2004. The influence of melt structure on trace element par-
1140 titioning near the peridotite solidus. Contributions to Mineralogy and
1141 Petrology 147, 511–527. doi:10.1007/s00410-004-0575-1.
- 1142 Gaetani, G.A., Grove, T.L., 1995. Partitioning of rare earth elements between
1143 clinopyroxene and silicate melt: Crystal-chemical controls. Geochimica et
1144 Cosmochimica Acta 59, 1951–1962. doi:10.1016/0016-7037(95)00119-0.
- 1145 Gaillard, F., Scaillet, B., Pichavant, M., 2002. Kinetics of iron oxidation-
1146 reduction in hydrous silicic melts. American Mineralogist 87, 829–837.
1147 doi:10.2138/am-2002-0704.
- 1148 Giehl, C., Marks, M., Nowak, M., 2013. Phase relations and liquid lines
1149 of descent of an iron-rich peralkaline phonolitic melt: an experimen-
1150 tal study. Contributions to Mineralogy and Petrology 165, 283–304.
1151 doi:10.1007/s00410-012-0809-6.
- 1152 Giordano, D., Nichols, A., Dingwell, D., 2005. Glass transition temperatures
1153 of natural hydrous melts: a relationship with shear viscosity and impli-
1154 cations for the welding process. Journal of Volcanology and Geothermal
1155 Research 142, 105–118. doi:10.1016/j.jvolgeores.2004.10.015.
- 1156 Girnis, A.V., Bulatov, V.K., Brey, G.P., Gerdes, A., Höfer, H.E., 2013. Trace
1157 element partitioning between mantle minerals and silico-carbonate melts
1158 at 6–12 GPa and applications to mantle metasomatism and kimberlite
1159 genesis. Lithos 160-161, 183–200. doi:10.1016/j.lithos.2012.11.027.

- 1160 Goodenough, K.M., Schilling, J., Jonsson, E., Kalvig, P., Charles, N., Tuduri,
1161 J., Deady, E.A., Sadeghi, M., Schiellerup, H., Müller, A., Bertrand, G.,
1162 Arvanitidis, N., Eliopoulos, D.G., Shaw, R.A., Thrane, K., Keulen, N.,
1163 2016. Europe's rare earth element resource potential: An overview of
1164 REE metallogenetic provinces and their geodynamic setting. *Ore Geology*
1165 *Reviews* 72, 838–856. doi:10.1016/j.oregeorev.2015.09.019.
- 1166 Grove, T.L., Baker, M.B., Kinzler, R.J., 1984. Coupled CaAl-NaSi dif-
1167 fusion in plagioclase feldspar: Experiments and applications to cooling
1168 rate speedometry. *Geochimica et Cosmochimica Acta* 48, 2113–2121.
1169 doi:10.1016/0016-7037(84)90391-0.
- 1170 Guillou, H., Carracedo, J.C., Paris, R., Pérèz Torrado, F.J., 2004. Implica-
1171 tions for the early shield-stage evolution of Tenerife from K/Ar ages and
1172 magnetic stratigraphy. *Earth and Planetary Science Letters* 222, 599–614.
1173 doi:10.1016/j.epsl.2004.03.012.
- 1174 Gurenko, A.A., Hoernle, K.A., Hauff, F., Schmincke, H.U., Han, D., Miura,
1175 Y.N., Kaneoka, I., 2006. Major, trace element and NdSrPbOHeAr isotope
1176 signatures of shield stage lavas from the central and western Canary Is-
1177 lands: Insights into mantle and crustal processes. *Chemical Geology* 233,
1178 75–112. doi:10.1016/j.chemgeo.2006.02.016.
- 1179 Hanchar, J.M., Finch, R.J., Hoskin, P.W.O., Watson, E.B., Cher-
1180 niak, D.J., Mariano, A.N., 2001. Rare earth elements in synthetic
1181 zircon: Part 1. Synthesis, and rare earth element and phospho-
1182 rus doping. *American Mineralogist* 86, 667–680. doi:10.1130/0091-
1183 7613(1990)018;0757:CTOGAS;2.3.CO;2.

- 1184 Hazen, R.M., Finger, L.W., 1979. Bulk modulus-volume relationship for
1185 cation-anion polyhedra. *Journal of Geophysical Research: Solid Earth* 84,
1186 6723–6728. doi:10.1029/JB084iB12p06723.
- 1187 Hill, E., Blundy, J.D., Wood, B.J., 2011. Clinopyroxene-melt trace ele-
1188 ment partitioning and the development of a predictive model for HFSE
1189 and Sc. *Contributions to Mineralogy and Petrology* 161, 423–438.
1190 doi:10.1007/s00410-010-0540-0.
- 1191 Hill, E., Wood, B.J., Blundy, J.D., 2000. The effect of Ca-Tschermaks com-
1192 ponent on trace element partitioning between clinopyroxene and silicate
1193 melt. *Lithos* 53, 203–215. doi:10.1016/S0024-4937(00)00025-6.
- 1194 Huang, F., Lundstrom, C.C., McDonough, W.F., 2006. Effect of melt
1195 structure on trace-element partitioning between clinopyroxene and sili-
1196 cic, alkaline, aluminous melts. *American Mineralogist* 91, 1385–1400.
1197 doi:10.2138/am.2006.1909.
- 1198 Jugo, P.J., Wilke, M., Botcharnikov, R.E., 2010. Sulfur K-edge XANES anal-
1199 ysis of natural and synthetic basaltic glasses: Implications for S speciation
1200 and S content as function of oxygen fugacity. *Geochimica et Cosmochimica
1201 Acta* 74, 5926–5938. doi:10.1016/j.gca.2010.07.022.
- 1202 Kennedy, A.K., Lofgren, G.E., Wasserburg, G.J., 1993. An experimental
1203 study of trace element partitioning between olivine, orthopyroxene and
1204 melt in chondrules: equilibrium values and kinetic effects. *Earth and Plan-
1205 etary Science Letters* 115, 177–195. doi:10.1016/0012-821X(93)90221-T.

- 1206 Kogarko, L.N., 1990. Ore-forming potential of alkaline magmas. *Lithos* 26,
1207 167–175. doi:10.1016/0024-4937(90)90046-4.
- 1208 Kovalenko, V.I., Hervig, R.L., Sheridan, M.F., 1988. Ion microprobe anal-
1209 yses of trace elements in anorthoclase, hedenbergite, aenigmatite, quartz,
1210 apatite and glass in pantellerite: evidence for high water contents in pan-
1211 tellerite melt. *American Mineralogist* 73, 1038–1045.
- 1212 Kress, V.C., Carmichael, I.S.E., 1991. The compressibility of silicate liquids
1213 containing Fe₂O₃ and the effect of composition, temperature, oxygen fu-
1214 gacity and pressure on their redox states. *Contributions to Mineralogy and*
1215 *Petrology* 108, 82–92. doi:10.1007/BF00307328.
- 1216 Kumazawa, M., 1969. The elastic constants of single-crystal or-
1217 thopyroxene. *Journal of Geophysical Research* 74, 5973–5980.
1218 doi:10.1029/JB074i025p05973.
- 1219 Larsen, L.M., 1979. Distribution of REE and other trace elements between
1220 phenocrysts and peralkaline undersaturated magmas, exemplified by rocks
1221 from the Gardar igneous province, south Greenland. *Lithos* 12, 303–315.
1222 doi:10.1016/0024-4937(79)90022-7.
- 1223 Law, K.M., Blundy, J.D., Wood, B.J., Ragnarsdottir, K.V., 2000. Trace ele-
1224 ment partitioning between wollastonite and silicate-carbonate melt. *Min-
1225 eralogical Magazine* 64, 651–661. doi:10.1180/002646100549670.
- 1226 Liang, Y., Richter, F.M., Watson, E.B., 1994. Convection in multicom-
1227 ponent silicate melts driven by coupled diffusion. *Nature* 369, 390–392.
1228 doi:10.1038/369390a0.

- 1229 Linnen, R.L., Keppler, H., 1997. Columbite solubility in granitic melts:
1230 consequences for the enrichment and fractionation of Nb and Ta in the
1231 Earth's crust. Contributions to Mineralogy and Petrology 128, 213–227.
1232 doi:10.1007/s004100050304.
- 1233 Lofgren, G., 1989. Dynamic crystallization of chondrule melts of porphyritic
1234 olivine composition: Textures experimental and natural. Geochimica et
1235 Cosmochimica Acta 53, 461–470. doi:10.1016/0016-7037(89)90397-9.
- 1236 Lofgren, G.E., Huss, G.R., Wasserburg, G.J., 2006. An experimental study
1237 of trace-element partitioning between Ti-Al-clinopyroxene and melt: Equi-
1238 librium and kinetic effects including sector zoning. American Mineralogist
1239 91, 1596–1606. doi:10.2138/am.2006.2108.
- 1240 Lu, F., Anderson, A.T., Davis, A.M., 1995. Diffusional gradients at the crys-
1241 tal / melt interface and their effect on the compositions of melt inclusions.
1242 The Journal of Geology 103, 591–597.
- 1243 Lundstrom, C.C., Shaw, H.F., Ryerson, F.J., Phinney, D.L., Gill, J.B.,
1244 Williams, Q., 1994. Compositional controls on the partitioning of U, Th,
1245 Ba, Pb, Sr and Zr between clinopyroxene and haplobasaltic melts: impli-
1246 cations for uranium series disequilibria in basalts. Earth and Planetary
1247 Science Letters 128, 407–423. doi:10.1016/0012-821X(94)90159-7.
- 1248 Mahood, G.A., Stimac, J.A., 1990. Trace-element partitioning in pantel-
1249 lerites and trachytes. Geochimica et Cosmochimica Acta 54, 2257–2276.
1250 doi:10.1016/0016-7037(90)90050-U.

- 1251 Marks, M., Halama, R., Wenzel, T., Markl, G., 2004. Trace element vari-
1252 ations in clinopyroxene and amphibole from alkaline to peralkaline syen-
1253 ites and granites: implications for mineral-melt trace-element partitioning.
1254 Chemical Geology 211, 185–215. doi:10.1016/j.chemgeo.2004.06.032.
- 1255 Marks, M., Markl, G., 2001. Fractionation and assimilation processes in the
1256 alkaline augite syenite unit of the Ilímaussaq intrusion, south Greenland,
1257 as deduced from phase equilibria. Journal of Petrology 42, 1947–1969.
1258 doi:10.1093/petrology/42.10.1947.
- 1259 Marks, M., Markl, G., 2003. Ilímaussaq en miniature': closed-system frac-
1260 tionation in an agpaitic dyke rock from the Gardar Province, South Green-
1261 land (contribution to the mineralogy of Ilímaussaq no. 117). Mineralogical
1262 Magazine 67, 893–919. doi:10.1180/0026461036750150.
- 1263 Marks, M.A., Markl, G., 2017. A global review on agpaitic rocks. Earth-
1264 Science Reviews 173, 229–258. doi:10.1016/j.earscirev.2017.06.002.
- 1265 Marks, M.A.W., Hettmann, K., Schilling, J., Frost, B.R., Markl, G., 2011.
1266 The mineralogical diversity of alkaline igneous rocks: Critical factors for
1267 the transition from miaskitic to agpaitic phase assemblages. Journal of
1268 Petrology 52, 439–455. doi:10.1093/petrology/egq086.
- 1269 Möller, V., Williams-Jones, A.E., 2016. Petrogenesis of the Necha-
1270 lacho Layered Suite, Canada: magmatic evolution of a REE-Nb-
1271 rich nepheline syenite intrusion. Journal of Petrology 57, 229–276.
1272 doi:10.1093/petrology/egw003.

- 1273 Mollo, S., Blundy, J.D., Giacomoni, P., Nazzari, M., Scarlato, P., Coltorti,
1274 M., Langone, A., Andronico, D., 2017. Clinopyroxene-melt element par-
1275 titioning during interaction between trachybasaltic magma and siliceous
1276 crust: Clues from quartzite enclaves at Mt. Etna volcano. *Lithos* 284–285,
1277 447–461. doi:10.1016/j.lithos.2017.05.003.
- 1278 Mollo, S., Blundy, J.D., Iezzi, G., Scarlato, P., Langone, A., 2013. The
1279 partitioning of trace elements between clinopyroxene and trachybasaltic
1280 melt during rapid cooling and crystal growth. *Contributions to Mineralogy*
1281 and Petrology
- 1282 166, 1633–1654. doi:10.1007/s00410-013-0946-6.
- 1283 Mollo, S., Forni, F., Bachmann, O., Blundy, J.D., De Astis, G., Scarlato,
1284 P., 2016. Trace element partitioning between clinopyroxene and trachy-
1285 phonolitic melts: A case study from the Campanian Ignimbrite (Campi
Flegrei, Italy). *Lithos* 252253, 160–172. doi:10.1016/j.lithos.2016.02.024.
- 1286 Moore, G., Vennemann, T., Carmichael, I.S.E., 1998. An empirical model
1287 for the solubility of H₂O in magmas to 3 kilobars. *American Mineralogist*
1288 83, 36–42. doi:10.1016/0012-821X(73)90129-5.
- 1289 Morimoto, N., 1989. Nomenclature of pyroxenes. *Mineralogical Journal* 14,
1290 198–221. doi:10.2465/minerj.14.198.
- 1291 Mungall, J., Brenan, J., 2014. Partitioning of platinum-group elements and
1292 Au between sulfide liquid and basalt and the origins of mantle-crust frac-
1293 tionation of the chalcophile elements. *Geochimica et Cosmochimica Acta*
1294 125, 265–289. doi:10.1016/j.gca.2013.10.002.

- 1295 Mysen, B.O., Virgo, D., Seifert, F.A., 1982. The structure of silicate melts:
1296 Implications for chemical and physical properties of natural magma. Re-
1297 views of Geophysics 20, 353–383. doi:10.1029/RG020i003p00353.
- 1298 Mysen, B.O., Virgo, D., Seifert, F.A., 1985. Relationships between properties
1299 and structure of aluminosilicate melts. American Mineralogist 70, 88–105.
1300 doi:10.1007/BF00413348.
- 1301 Niu, Y., 2004. Bulk-rock major and trace element compositions of abyssal
1302 peridotites: Implications for mantle melting, melt extraction and post-
1303 melting processes beneath Mid-Ocean ridges. Journal of Petrology 45,
1304 2423–2458. doi:10.1093/petrology/egh068.
- 1305 Olin, P.H., Wolff, J.A., 2010. Rare earth and high field strength element par-
1306 titioning between iron-rich clinopyroxenes and felsic liquids. Contributions
1307 to Mineralogy and Petrology 160, 761–775. doi:10.1007/s00410-010-0506-2.
- 1308 Onuma, N., Higuchi, H., Wakita, H., Nagasawa, H., 1968. Trace element
1309 partition between two pyroxenes and the host lava. Earth and Planetary
1310 Science Letters 5, 47–51. doi:10.1016/S0012-821X(68)80010-X.
- 1311 Paton, C., Hellstrom, J., Paul, B., Woodhead, J., Herdt, J., 2011. Io-
1312 lite: Freeware for the visualisation and processing of mass spectromet-
1313 ric data. Journal of Analytical Atomic Spectrometry 26, 2508–2518.
1314 doi:10.1039/C1JA10172B.
- 1315 Peters, S.T., Troll, V.R., Weis, F.A., Dallai, L., Chadwick, J.P., Schulz, B.,
1316 2017. Amphibole megacrysts as a probe into the deep plumbing system

- 1317 of Merapi volcano, Central Java, Indonesia. Contributions to Mineralogy
1318 and Petrology 172, 1–20. doi:10.1007/s00410-017-1338-0.
- 1319 Prowatke, S., Klemme, S., 2005. Effect of melt composition on the parti-
1320 tioning of trace elements between titanite and silicate melt. Geochimica
1321 et Cosmochimica Acta 69, 695–709. doi:10.1016/j.gca.2004.06.037.
- 1322 Putirka, K.D., 2008. Thermometers and Barometers for Volcanic
1323 Systems. Reviews in Mineralogy and Geochemistry 69, 61–120.
1324 doi:10.2138/rmg.2008.69.3.
- 1325 Rapp, R.P., Watson, E.B., 1986. Monazite solubility and dissolution ki-
1326 netics: implications for the thorium and light rare earth chemistry of
1327 felsic magmas. Contributions to Mineralogy and Petrology 94, 304–316.
1328 doi:10.1007/BF00371439.
- 1329 Rasband, W., 2016. ImageJ, U.S. National Institutes of Health, Bethesda,
1330 Maryland, USA.
- 1331 Redhammer, G.J., Amthauer, G., Roth, G., Tippelt, G., Lotter-
1332 moser, W., 2006. Single-crystal X-ray diffraction and temperature
1333 dependent ^{57}Fe Mössbauer spectroscopy on the hedenbergite-aegirine
1334 $(\text{Ca},\text{Na})(\text{Fe}^{2+},\text{Fe}^{3+})\text{Si}_2\text{O}_6$ solid solution. American Mineralogist 91,
1335 1271–1292. doi:10.2138/am.2006.2173.
- 1336 Reguir, E.P., Chakhmouradian, A.R., Pisiak, L., Halden, N.M., Yang, P.,
1337 Xu, C., Kynický, J., Couëslan, C.G., 2012. Trace-element composition
1338 and zoning in clinopyroxene- and amphibole-group minerals: Implications

- 1339 for element partitioning and evolution of carbonatites. *Lithos* 128, 27–45.
1340 doi:10.1016/j.lithos.2011.10.003.
- 1341 Rubatto, D., Hermann, J., 2007. Experimental zircon/melt and
1342 zircon/garnet trace element partitioning and implications for the
1343 geochronology of crustal rocks. *Chemical Geology* 241, 38–61.
1344 doi:10.1016/j.chemgeo.2007.01.027.
- 1345 Schmidt, B.C., Behrens, H., 2008. Water solubility in phonolite melts: Influ-
1346 ence of melt composition and temperature. *Chemical Geology* 256, 259–
1347 268. doi:10.1016/j.chemgeo.2008.06.043.
- 1348 Schmidt, K.H., Bottazzi, P., Vannucci, R., Mengel, K., 1999. Trace element
1349 partitioning between phlogopite, clinopyroxene and leucite lamproite melt.
1350 *Earth and Planetary Science Letters* 168, 287–299. doi:10.1016/S0012-
1351 821X(99)00056-4.
- 1352 Schmidt, M.W., Connolly, J.A.D., Günther, D., Bogaerts, M., 2006. Element
1353 partitioning: The role of melt structure and composition. *Science* 312,
1354 1646–1650. doi:10.1126/science.1126690.
- 1355 Severs, M.J., Beard, J.S., Fedele, L., Hanchar, J.M., Mutchler, S.R., Bodnar,
1356 R.J., 2009. Partitioning behavior of trace elements between dacitic melt
1357 and plagioclase, orthopyroxene, and clinopyroxene based on laser ablation
1358 ICPMS analysis of silicate melt inclusions. *Geochimica et Cosmochimica
1359 Acta* 73, 2123–2141. doi:10.1016/j.gca.2009.01.009.
- 1360 Shannon, R., 1976. Revised effective ionic radii and systematic studies of

- 1361 interatomic distances in halides and chalcogenides. *Acta Crystallographica*
1362 Section A 32, 751–767.
- 1363 Shea, T., Hammer, J.E., 2013. Kinetics of cooling- and decompression-
1364 induced crystallization in hydrous mafic-intermediate magmas.
1365 *Journal of Volcanology and Geothermal Research* 260, 127–145.
1366 doi:10.1016/j.jvolgeores.2013.04.018.
- 1367 Shearer, C.K., Larsen, L.M., 1994. Sector-zoned aegirine from the Ilimaussaq
1368 alkaline intrusion, South Greenland; implications for trace-element behav-
1369 ior in pyroxene. *American Mineralogist* 79, 340–352.
- 1370 Sjöqvist, A., Cornell, D., Andersen, T., Erambert, M., Ek, M., Leijd, M.,
1371 2013. Three compositional varieties of rare-earth element ore: Eudialyte-
1372 group minerals from the Norra Kärr alkaline complex, Southern Sweden.
1373 *Minerals* 3, 94–120. doi:10.3390/min3010094.
- 1374 Sørensen, H., 1992. Agpaitic nepheline syenites: a potential source of
1375 rare elements. *Applied Geochemistry* 7, 417–427. doi:10.1016/0883-
1376 2927(92)90003-L.
- 1377 Spera, F.J., Bohrson, W.A., 2001. Energy-constrained open-system mag-
1378 matic processes I: General model and energy-constrained assimilation and
1379 fractional crystallization (EC-AFC) formulation. *Journal of Petrology* 42,
1380 999–1018. doi:10.1093/petrology/42.5.999.
- 1381 Stevens, J., 1996. Applied multivariate analysis for the social sciences.
1382 Lawrence Erlbaum, Mahwah, NJ.

- 1383 Sun, C., Liang, Y., 2012. Distribution of REE between clinopyroxene and
1384 basaltic melt along a mantle adiabat: Effects of major element composi-
1385 tion, water, and temperature. Contributions to Mineralogy and Petrology
1386 163, 807–823. doi:10.1007/s00410-011-0700-x.
- 1387 Thirlwall, M.F., Singer, B.S., Marriner, G.F., 2000. ^{39}Ar – ^{40}Ar ages and
1388 geochemistry of the basaltic shield stage of Tenerife, Canary Islands,
1389 Spain. Journal of Volcanology and Geothermal Research 103, 247–297.
1390 doi:10.1016/S0377-0273(00)00227-4.
- 1391 Troll, V., Schmincke, H., 2002. Magma mixing and crustal recycling recorded
1392 in ternary feldspar from compositionally zoned peralkaline ignimbrite
1393 'A', Gran Canaria, Canary Islands. Journal of Petrology 43, 243–270.
1394 doi:10.1093/petrology/43.2.243.
- 1395 Van Orman, J.A., Grove, T.L., Shimizu, N., 2001. Rare earth element diffu-
1396 sion in diopside: influence of temperature, pressure, and ionic radius, and
1397 an elastic model for diffusion in silicates. Contributions to Mineralogy and
1398 Petrology 141, 687–703. doi:10.1007/s004100100269.
- 1399 Walker, D., Kirkpatrick, R.J., Longhi, J., Hays, J.F., 1976. Crystallization
1400 history of lunar picritic basalt sample 12002: Phase-equilibria and cooling-
1401 rate studies. Bulletin of the Geological Society of America 87, 646–656.
1402 doi:10.1130/0016-7606(1976)87;646:CHOLPB;2.0.CO;2.
- 1403 Watson, E.B., 1979. Zircon saturation in felsic liquids: Experimental results
1404 and applications to trace element geochemistry. Contributions to Miner-
1405 alogy and Petrology 70, 407–419. doi:10.1007/BF00371047.

- 1406 Weidner, D.J., Vaughan, M.T., 1982. Elasticity of pyroxenes: Effects of
1407 composition versus crystal structure. *Journal of Geophysical Research* 87,
1408 9349–9353.
- 1409 Wiesmaier, S., Troll, V.R., Carracedo, J.C., Ellam, R.M., Bindeman, I.,
1410 Wolff, J.A., 2012. Bimodality of lavas in the Teide–Pico Viejo Succession
1411 in Tenerife—the role of crustal melting in the origin of recent phonolites.
1412 *Journal of Petrology* 53, 2465–2495. doi:10.1093/petrology/egs056.
- 1413 Wood, B.J., Blundy, J.D., 1997. A predictive model for rare earth
1414 element partitioning between clinopyroxene and anhydrous silicate
1415 melt. *Contributions to Mineralogy and Petrology* 129, 166–181.
1416 doi:10.1007/s004100050330.
- 1417 Wood, B.J., Blundy, J.D., 2001. The effect of cation charge on crystal–melt
1418 partitioning of trace elements. *Earth and Planetary Science Letters* 188,
1419 59–71. doi:10.1016/S0012-821X(01)00294-1.
- 1420 Wood, B.J., Blundy, J.D., 2003. Trace element partitioning under crustal
1421 and uppermost mantle conditions: The influences of ionic radius, cation
1422 charge, pressure, and temperature, in: Carlson, R.W. (Ed.), *The Mantle*
1423 and Core: Treatise on Geochemistry. Elsevier. volume 2. chapter 2.09, pp.
1424 395–424. doi:10.1016/B0-08-043751-6/02009-0.
- 1425 Wood, B.J., Blundy, J.D., 2014. Trace element partitioning: The influences
1426 of ionic radius, cation charge, pressure, and temperature, in: Carlson,
1427 R.W. (Ed.), *The Mantle and Core: Treatise on Geochemistry: Second Edi-*

- 1428 tion. Elsevier. chapter 3.11, pp. 421–445. doi:10.1016/B978-0-08-095975-
1429 7.00206-0.
- 1430 Wood, B.J., Trigila, R., 2001. Experimental determination of aluminous
1431 clinopyroxene–melt partition coefficients for potassic liquids, with applica-
1432 tion to the evolution of the Roman province potassic magmas. Chemical
1433 Geology 172, 213–223. doi:10.1016/S0009-2541(00)00259-X.
- 1434 Workman, R.K., Hart, S.R., 2005. Major and trace element composition of
1435 the depleted MORB mantle (DMM). Earth and Planetary Science Letters
1436 231, 53–72. doi:10.1016/j.epsl.2004.12.005.
- 1437 Wörner, G., Beusen, J.M., Duchateau, N., Gijbels, R., Schmincke, H.U.,
1438 1983. Trace element abundances and mineral/melt distribution coefficients
1439 in phonolites from the Laacher See volcano (Germany). Contributions to
1440 Mineralogy and Petrology 84, 152–173. doi:10.1007/BF00371282.
- 1441 Xu, C., Kynicky, J., Chakhmouradian, A.R., Campbell, I.H., Allen, C.M.,
1442 2010. Trace-element modeling of the magmatic evolution of rare-earth-rich
1443 carbonatite from the Miaoya deposit, Central China. Lithos 118, 145–155.
1444 doi:10.1016/j.lithos.2010.04.003.
- 1445 Yang, L., van Hinsberg, V.J., Samson, I.M., 2018. Some data reduction meth-
1446 ods for laser ablation analyses of difficult samples. Submitted manuscript
1447 .
- 1448 Yao, L., Sun, C., Liang, Y., 2012. A parameterized model for REE distri-
1449 bution between low-Ca pyroxene and basaltic melts with applications to

¹⁴⁵⁰ REE partitioning in low-Ca pyroxene along a mantle adiabat and dur-
¹⁴⁵¹ ing pyroxenite-derived melt and peridotite interaction. Contributions to
¹⁴⁵² Mineralogy and Petrology 164, 261–280. doi:10.1007/s00410-012-0737-5.

¹⁴⁵³ Zhang, Y., Ni, H., Chen, Y., 2010. Diffusion data in silicate melts. Reviews
¹⁴⁵⁴ in Mineralogy and Geochemistry 72, 311–408. doi:10.2138/rmg.2010.72.8.

¹⁴⁵⁵ **6. Tables**

Table 1: Major-element composition (in wt%) of starting materials for the internally heated pressure vessel experiments. The totals are calculated with all iron as FeO.

Dry starting glass compositions calculated from masses of reagents added [wt%]

Composition	SiO ₂	TiO ₂	Al ₂ O ₃	FeOT	MgO	CaO	Na ₂ O	K ₂ O	Total	(Na+K)/Al
L4	57.48	1.50	19.00	5.89	1.61	3.21	7.33	3.98	100.00	0.861
L5	61.24	0.68	19.51	3.77	0.43	0.91	8.63	4.84	100.00	0.996
M3	52.67	2.27	18.13	7.86	2.75	5.40	7.19	3.73	100.00	0.875
M4	56.35	1.47	18.63	5.77	1.58	3.15	8.48	4.57	100.00	1.014
M5	60.04	0.66	19.13	3.69	0.42	0.89	9.76	5.41	100.00	1.145
H4	54.80	1.43	18.12	5.62	1.54	3.06	10.07	5.38	100.00	1.236
H5	58.38	0.65	18.60	3.59	0.41	0.86	11.31	6.20	100.00	1.362

Water saturated glass compositions from superliquidus experiments (EPMA) [wt%]

L5	57.46	0.643	16.59	2.363	0.404	0.985	7.840	4.462	90.75	1.069
s.d. (n = 8)	0.299	0.087	0.210	0.059	0.035	0.050	0.175	0.132	0.351	0.017
rsd	0.52%	13.58%	1.26%	2.51%	8.70%	5.09%	2.23%	2.97%	0.39%	1.57%
H5	55.58	0.612	16.21	2.568	0.422	0.906	10.77	5.732	92.80	1.476
s.d. (n = 13)	0.327	0.057	0.221	0.113	0.044	0.049	0.205	0.154	0.417	0.028
rsd	0.59%	9.33%	1.36%	4.41%	10.44%	5.40%	1.90%	2.69%	0.45%	1.87%

Table 2: Summary of run conditions and run products for the internally-heated pressure vessel experiments.

Experiment	Setup	Pressure [bar]	Cooling ramp				(after ramp) [h,m]	Run products
			Rate °C /min	Cycle +10°C	TE-1/TE-3 [°C]	TE-2 (spl) [°C]		
L4 ₃	IHPV RQ (f)	2038	1	Y	825	828	44h50m	Cpx + Ox + Ttn + Melt
L5 ₃	IHPV RQ (f)	2038	1	Y	825	828	44h50m	Cpx + Ox + Melt
M3 ₂	IHPV RQ	2020	1	Y	796/795	799	47h	Cpx + Ox + Bt + Melt
M4 ₄	IHPV RQ	2020	1	Y	796/795	799	47h	Cpx + Ox + Bt + Melt
M5	IHPV	2000	-	-	800	799	47h55m	Cpx + Bt + Fsp + Melt
M5 ₂	IHPV RQ	2000	-	-	700	689	45h45m	Cpx + Bt + Fsp + Melt
H4 ₂	IHPV	2000	-	-	800	799	47h55m	Cpx + Ttn + Melt
H5 ₂	IHPV RQ	2000	-	-	700	689	45h45m	Cpx + Bt + Fsp + Melt
H5 ₃	IHPV RQ	2020	-	-	651/649	648	46h15m	Cpx + Bt + Fsp + Melt
NLS-9	IHPV RQ	2020	1	Y	651/649	648	46h15m	Cpx + Ox + Melt
NLS-9 ₂ HM	IHPV RQ**	2000	1	Y	650	655	42h	Cpx + Ox + Fsp + Melt

(f) indicates failure of the rapid quench apparatus; ** indicates use of a haematite double capsule, for run conditions at the haematite-magnetite $f\text{O}_2$ buffer (Eugster and Wones, 1962). Cpx = clinopyroxene; Ox = spinel oxide; Ttn = titanite; Bt = biotite; Fsp = sanidine feldspar.

Table 3: Representative major-element compositions of clinopyroxene and melt for the performed internally heated pressure vessel experiments and Canary Islands phenocryst–glass pairs.

<i>Pyroxene</i>	L4 ₃	M3 ₂	M5 ₂	H5 ₃	NLS-9	NLS-9 ₂ HM	16-07 LMB	17-12 M. Samara	17-14 UMB-II	21-30 PV 2 ka
SiO ₂	44.70	40.73	47.31	46.95	50.73	51.90	52.43	51.77	51.81	52.50
TiO ₂	3.07	4.57	3.17	4.47	0.10	0.10	0.80	0.78	0.74	0.75
Al ₂ O ₃	5.23	9.26	3.08	3.10	2.46	2.96	1.33	1.24	1.27	1.22
FeO	13.31	11.72	18.84	16.95	28.14	28.61	9.71	9.62	10.51	10.02
MnO	0.01	0.01	0.01	0.00	0.25	0.17	0.78	0.84	0.91	0.81
MgO	9.09	9.28	5.55	6.05	0.05	0.07	12.30	12.64	12.07	11.88
CaO	19.49	22.17	16.11	15.29	5.88	3.14	21.90	21.76	21.52	22.02
Na ₂ O	2.27	1.01	4.34	4.97	9.86	11.45	1.18	1.17	1.38	1.19
K ₂ O	0.09	0.03	0.08	0.07	0.04	0.04	0.02	0.03	0.00	0.02
Total	97.25	98.78	98.49	97.85	97.49	98.45	100.44	99.85	100.22	100.42
<i>Glass</i>										
SiO ₂	58.79	57.29	57.45	54.91	58.17	58.14	60.38	55.10	59.08	60.04
TiO ₂	0.35	0.27	0.23	0.62	0.00	0.00	0.64	1.73	0.66	0.66
Al ₂ O ₃	17.35	19.14	16.69	16.06	18.55	19.41	19.96	18.30	19.68	19.79
Fe ₂ O ₃ (T)	2.35	1.35	1.01	3.16	1.67	1.91	3.65	7.22	4.02	3.96
FeO(T)	2.12	1.22	0.91	2.84	1.50	1.72	3.28	6.49	3.62	3.56
MnO	0.02	0.00	-	0.01	0.06	0.04	0.14	0.23	0.22	0.20
MgO	0.20	0.13	0.15	0.35	0.00	0.00	0.39	1.84	0.32	0.35
CaO	0.55	0.95	0.24	0.84	0.23	0.23	0.76	4.10	0.77	0.74
Na ₂ O	7.17	7.32	9.08	8.88	11.12	9.80	9.00	7.26	9.76	9.05
K ₂ O	4.68	4.10	4.68	5.30	1.51	2.51	5.41	4.09	5.45	5.57
Total	91.23	90.41	89.43	89.81	91.15	91.85	99.95	99.13	99.56	99.95
(Na+K)/Al	0.97	0.86	1.15	1.27	1.07	0.97	1.01	1.12	1.09	1.09

Table 4: Pyroxene-melt trace-element-partition coefficients for representative experiments and a natural phenocryst-glass pair.

-	L4 ₃		M3 ₂		M5 ₂		H5 ₃		NLS-9		NLS-9 ₂ HM		16-07-px4 LMB	
	D	σ	D	σ	D	σ	D	σ	D	σ	D	σ	D	σ
Li	0.250	0.016	0.126	0.009	0.419	0.034	0.427	0.024	0.274	0.029	0.251	0.025	0.157	0.021
Ga	0.364	0.022	0.567	0.020	0.190	0.022	-	-	-	-	-	-	0.216	0.020
Rb	0.005	0.002	0.018	0.003	0.010	0.006	0.013	0.002	0.026	0.015	-	-	0.000	0.000
Sr	0.828	0.045	0.282	0.024	1.433	0.111	0.997	0.091	0.321	0.045	0.269	0.111	0.732	0.293
Y	5.577	0.302	13.784	1.949	1.814	0.236	1.102	0.060	0.482	0.048	0.713	0.070	2.183	0.232
Zr	1.699	0.082	2.537	0.222	1.361	0.089	1.164	0.083	2.102	0.196	3.895	0.482	0.434	0.047
Nb	0.126	0.085	0.889	0.258	0.554	0.280	1.688	0.196	2.382	0.294	9.642	4.015	0.0062	0.0004
Cs	0.019	0.003	0.019	0.003	0.014	0.006	0.010	0.002	-	-	0.023	0.017	0.001	0.001
Ba	0.0364	0.0087	0.0373	0.0152	0.0388	0.0261	0.0288	0.0091	-	-	-	-	0.00004	0.00004
La	4.787	0.646	2.591	0.240	4.658	0.962	3.049	0.132	0.410	0.037	0.542	0.043	0.769	0.071
Ce	7.199	0.756	6.229	0.646	5.199	1.073	3.190	0.129	0.377	0.028	0.547	0.061	1.591	0.120
Nd	16.105	1.537	28.430	4.210	6.454	1.630	3.759	0.147	0.579	0.054	0.925	0.114	2.632	0.155
Sm	17.843	1.414	47.245	7.699	5.215	1.293	3.113	0.137	0.388	0.070	0.767	0.182	3.522	0.421
Eu	16.403	1.341	53.195	8.181	4.743	1.132	2.900	0.133	0.275	0.082	0.682	0.192	3.372	0.196
Dy	9.027	0.537	27.082	3.925	2.619	0.460	1.521	0.073	0.329	0.057	0.388	0.088	2.798	0.220
Tm	4.773	0.261	9.067	0.903	2.937	0.279	1.567	0.097	1.330	0.145	2.860	0.890	1.846	0.182
Yb	4.797	0.249	7.015	0.600	3.937	0.296	2.281	0.152	2.564	0.346	8.004	3.116	1.978	0.186
Hf	2.385	0.162	3.556	0.472	1.802	0.118	1.141	0.123	2.443	0.275	3.702	0.479	0.769	0.065
Ta	0.496	0.152	2.3694	0.6244	0.6502	0.2545	1.5654	0.2337	2.1082	0.1764	3.6854	0.6561	0.0153	0.0013
Pb	0.079	0.017	0.0587	0.0152	0.1142	0.0349	0.0199	0.0130	0.0884	0.0280	0.0564	0.0536	0.0203	0.0040
Th	0.201	0.034	0.3565	0.0419	0.3172	0.0321	0.2892	0.0239	0.0798	0.0240	0.0709	0.0276	0.0040	0.0003
U	-	-	0.0512	0.0331	0.1261	0.0272	0.0196	0.0103	0.0460	0.0245	0.0834	0.0342	0.0022	0.0003

Table 5: Coefficients for prediction of lattice-strain parameters for clinopyroxene M1 and M2 sites from clinopyroxene composition, temperature and pressure. Fitted vs. predicted lattice-strain parameters and partition coefficients are in Figures 12–13 and full multiple linear regression reports are available as supplementary data file S4.

Model for $\text{Ln}D_0$ M2 site (n = 82)			Model for $\text{Ln}D_0$, M1 site (n = 16)		
Parameter	Coefficient	σ	Parameter	Coefficient	σ
Intercept	4.52	0.91	Intercept	5	1
M1Ti	6.8	3	TAl	4	0.5
M1Al - M1Fe ³⁺	1.6	0.6	M1Fe ²⁺	2.6	0.9
M2Fe ²⁺	-3.8	1.3	M2Na	-8	1
T [K]	-0.0035	0.0007	M2Ca	-3	2
TAl + TFe ³⁺	2.6	0.8			
R^2		0.647			0.959

Model for E_s , M2 site (n = 79)			Model for E_s , M1 site (n = 18)		
Parameter	Coefficient	σ	Parameter	Coefficient	σ
Intercept	247	44	Intercept	-2322	298
M1Al	-424	144	T [K]	3.2	0.4
M1Mg	-285	102	P [GPa]	-408	145
M1Ti	-1145	378	M1Mg	-800	212
M2Mg	-306	115			
P [GPa]	37	12			
TAl + TFe ³⁺	313	102			
XMg	336	102			
R^2		0.348			0.936

Model for r_0 , M2 site (n = 82)			Model for r_0 , M1 site (n = 16)		
Parameter	Coefficient	σ	Parameter	Coefficient	σ
Intercept	1.01	0.02	Intercept	0.79	0.03
M1Ti	0.16	0.05	P [GPa]	-0.017	0.005
M1Al-M1Fe ³⁺	-0.03	0.01	M2Mg	-0.48	0.06
M2Ca	0.09	0.02	M1Fe ³⁺	0.14	0.03
M2Na	0.14	0.02	M2Ca	-0.05	0.02
T [K]	-4.46E-05	1.22E-05			
R^2		0.846			0.987

1456 7. Supplementary figures

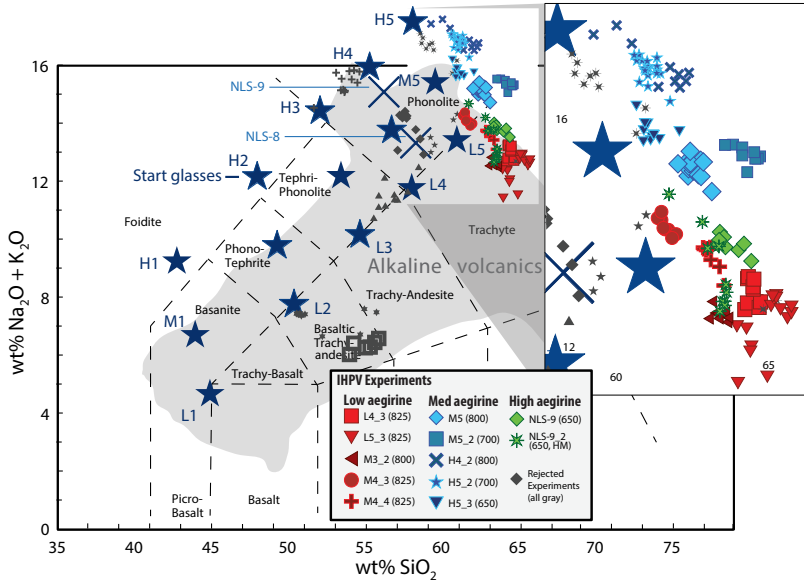


Figure S1: Total alkalies silica diagram for glasses produced in internally heated pressure vessel experiments. Large stars indicate synthetic starting glass compositions as used in internally heated pressure vessel experiments (Table 1). The gray field indicates the compositional range expressed by alkaline volcanic provinces from around the world, sourced from the GEOREM database. Full references in Supplement S1. Rejected experiments in dark gray are not discussed in the main text, and either did not produce clinopyroxene, produced crystals that were too small for analysis by LA-ICP-MS, or grew crystals during quench, hence preserving disequilibrium partitioning behaviour.

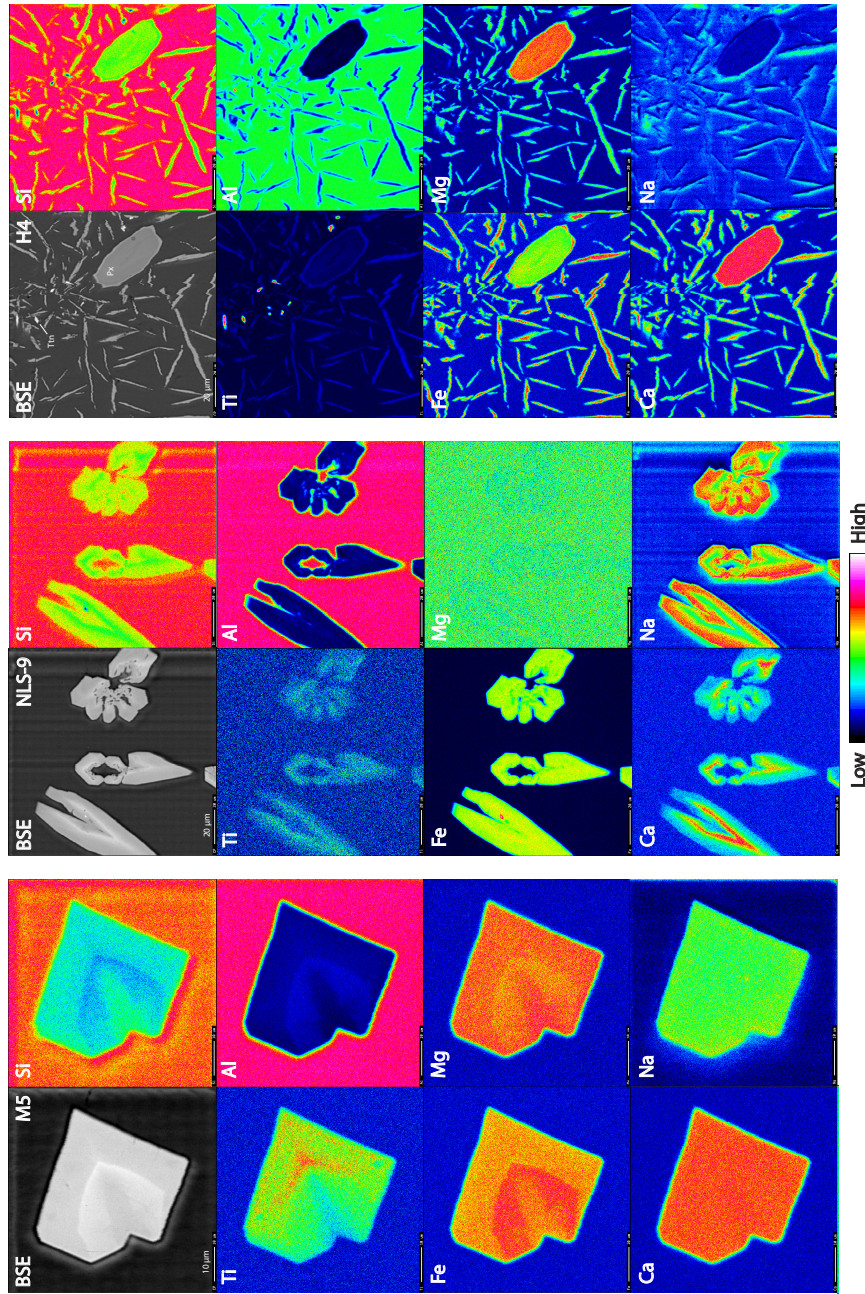


Figure S2: Element maps of clinopyroxene from internally heated pressure vessel experiments. M5 clinopyroxene have a sharp internal boundary that reflects feldspar saturation and are subtly zoned. NLS-9 clinopyroxene are more strongly zoned with swallowtail and hopper textures and rare inclusions of magnetite (cf. Walker et al., 1976; Lofgren, 1989; Shea and Hammer, 2013). H4 clinopyroxene (P_X) display a bimodal crystal size distribution and occur with titanite (Tn). The bimodal crystal size distribution is due to a temperature perturbation during run, and renders this experiment unsuitable for this element partitioning study.

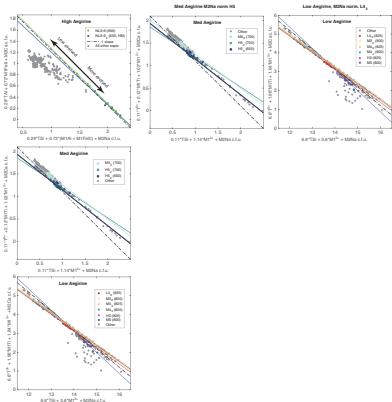


Figure S3: Major-element exchange mechanisms for (a) high, (b) medium and (c) low-aegirine clinopyroxene generated in internally heated pressure vessel experiments. Each individual plotted point represents an electron-microprobe analysis. Iron in the clinopyroxene was assigned to 2+ or 3+ valence following Droop (1987), then major-element cations were assigned to sites following Morimoto (1989, see supplement S5). Axes were defined by linear regressions between site-assigned major-element abundances, which have been checked for consistency in total site-occupancy and for charge.

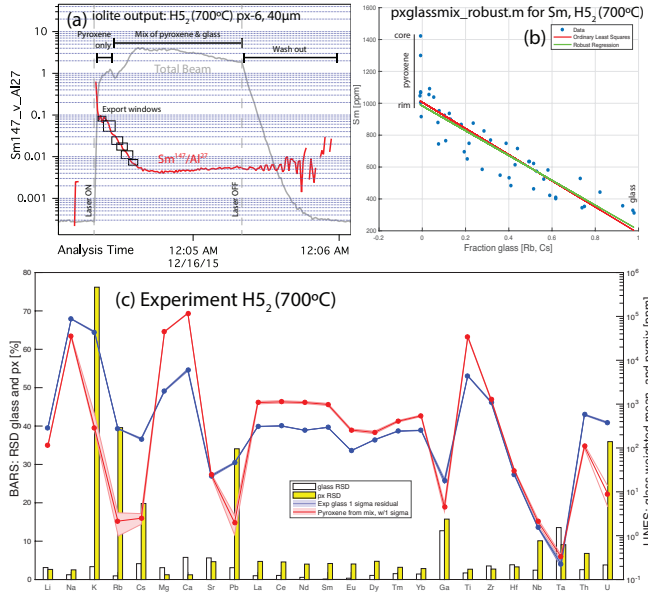


Figure S4: An example of the robust regression data reduction scheme for laser-ablation ICP-MS analyses of glass and clinopyroxene mixtures. (a) Time series of laser-ablation data, showing traces for Sm/Al (red) and total beam intensity (gray). The laser beam often ablated through the small clinopyroxene crystals, returning a mixed signal that was exported from the iolite data reduction software in short time windows as shown. Data were then normalised to the sum of major-element concentrations and mixes were deconvolved using a robust regression script written in MATLAB. (b) An example output diagram for the robust regression data reduction scheme. Clinopyroxene–glass mixing ratios were constrained by strongly incompatible elements Rb and Cs. For each element, a robust linear regression was defined between the fraction of glass in the mixture and element concentration. The intercept of this regression with zero glass returned the trace-element concentrations in the clinopyroxene. Uncertainty with this technique is typically below 10 % relative (median 9.3 % at the 1σ level). In this example, the Sm-rich core of a zoned clinopyroxene crystal is effectively rejected during data processing, and the derived Sm concentration for the clinopyroxene is therefore closer to that of the clinopyroxene rims that are in equilibrium with the adjacent quenched melt. (c) A quality control diagram output from the MATLAB data reduction scheme showing the concentrations of various elements in the glass and clinopyroxene (lines) and the uncertainty on these concentrations expressed as a relative standard deviation (BARS). Derived partition coefficients (D_i) are the mass concentration of element ' i ' in clinopyroxene divided by that in the adjacent quenched melt. Residuals for the D_i values were calculated using uncertainties derived from the clinopyroxene and glass analyses to calculate minimum and maximum partition coefficients at the 1σ level. These are reported in Table 4 and Supplement S1.

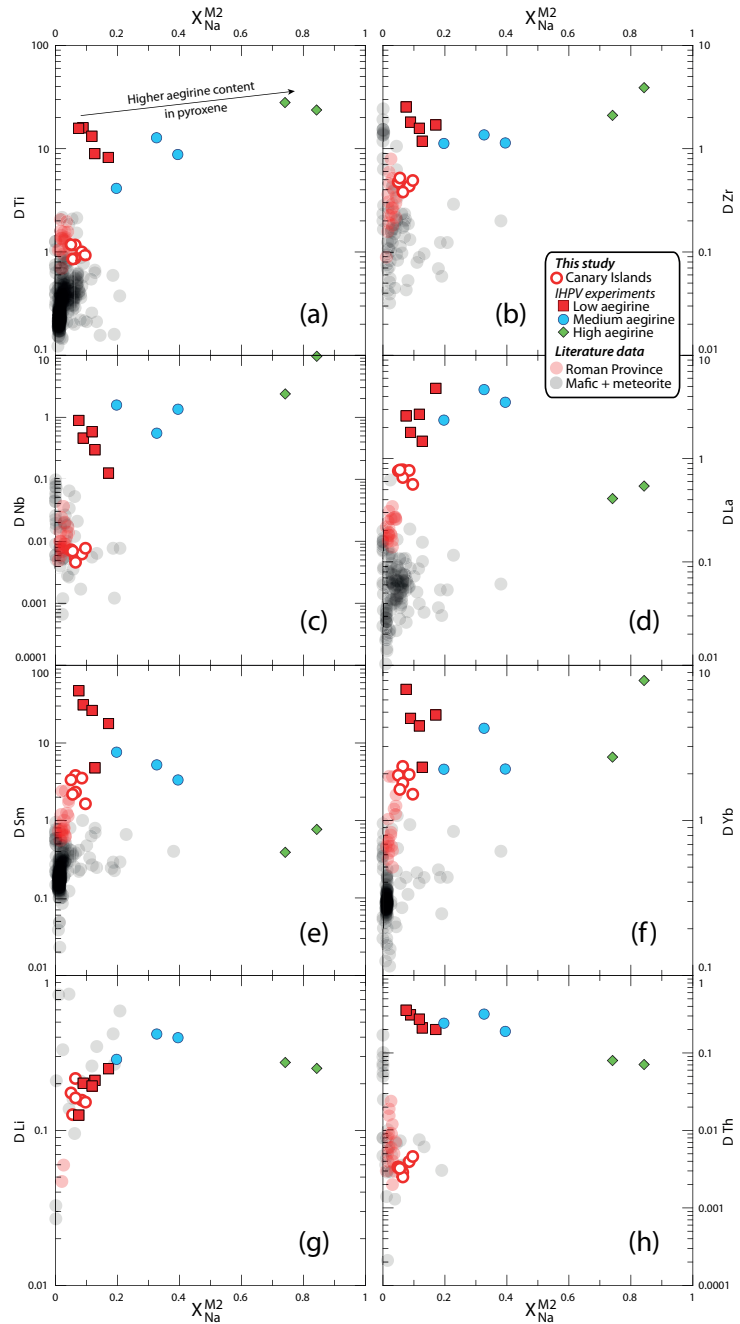


Figure S5: Element partitioning coefficients for HFSE (Ti, Zr, Nb), REE (La, Sm, Yb) and TE (Li, Th) vs. $X_{\text{Na}}^{\text{M}2}$. Literature values ($n = 411$), including those from the Roman Province, Italy, are from the compilation of Bédard (2014).

¹⁴⁵⁷ **8. Electronic appendices**

xlsx

Table S1: Electronic appendix (.xlsx file) containing experiment starting glass compositions, experiment run conditions, mineral abundances in experimental charges, compositions of reference materials used for EPMA and LA-ICP analyses, major-element concentrations for experiment glasses and clinopyroxene, partition coefficients and fitted lattice-strain parameters.

kml

Table S2: Electronic appendix (.kml file) containing field locations for the Canary Islands samples.

kml

Table S3: Electronic appendix (.xlsx file) containing electron-microprobe transects across experiment clinopyroxene for Ce, Mg and Fe. The data indicate that $D_{Ce}^{px/melt}$ values determined from our experiments are overestimates, but only by up to 25%. Sector zoning in the clinopyroxene appears to have a larger impact on apparent Ce partitioning behaviour than growth zoning.

pdf

Table S4: Electronic appendix (.pdf file) containing multiple linear regression reports from the stepwise fitting of 3+ cation lattice-strain parameters for the predictive model for element-partitioning (39 pages).

xlsx

Table S5: Electronic appendix (.xlsx file) containing a numerical model for prediction of clinopyroxene/melt element-partitioning coefficients for ions of 3+ valence. Required input data are major-element oxide compositions for clinopyroxene, pressure and temperature. The model for the M2 site is calibrated for application to systems of basaltic to peralkaline phonolite composition. The model for the M1 site is calibrated for use on alkaline to weakly peralkaline systems where the aegirine mol% in clinopyroxene does not exceed 50.